University of Helsinki Report Series in Physics

HU-P-D214

Atomistic simulations of metal surfaces under high electric fields

Stefan Parviainen

Division of Materials Physics
Department of Physics
Faculty of Science
University of Helsinki
Helsinki, Finland

Academic Dissertation

To be presented, with the permission of the Faculty of Science of the University of Helsinki, for public criticism in auditorium E204 of the Department of Physics (Physicum) on March 28th 2014 at 12 o'clock noon.

Helsinki 2014

Dedicated to the MS Comic Sans font

Osores oderint

ISBN 978-952-10-8952-7 (printed version)
ISSN 0356-0961
Tampere 2014
Juvenes Print

ISBN 978-952-10-8953-4 (PDF version)
http://ethesis.helsinki.fi/
Helsinki 2014
Electronic Publications @ University of Helsinki

Stefan Parviainen, **Atomistic simulations of metal surfaces under high electric fields**, University of Helsinki, 2014, 51 p.+appendices, Report Series in Physics HU-P-D214, ISSN 0356-0961, ISBN 978-952-10-8952-7 (printed version), ISBN 978-952-10-8953-4 (PDF version)

Abstract

Modern society runs largely on electricity, and where there is electricity there are electric fields. As the boundaries of technology are pushed forward, stronger and stronger electric fields are either required, or appear due to unwanted effects. Examples of such applications, where very high electric fields are utilised include particle accelerators and atom probes. To further be able to improve on such techniques, it is necessary to gain a good understanding of the processes that are involved. Because it is often difficult, if not impossible, to observe these processes with high resolution in experiments, one needs to consider the use of atomistic simulations instead.

This thesis provides an extension to classical molecular dynamics by describing an implementation where several electronic effects are considered when dealing with metal surfaces under high electric fields. These effects include the charging of surface atoms, field electron emission and the resulting resistive heating, as well as field evaporation of both neutral and charged atoms. In addition to the implementation details, the thesis also contains a brief background of the physics involved in these processes.

Using the implementation, it is observed that a surface protrusion may grow on an initially flat surface in the presence of a near-surface void when a strong external electric field is applied. The growth is very rapid, resulting finally catastrophic breakage. This mechanism may explain the appearance of field emitters on otherwise pristine samples, and the instability of measured field emission currents. Simulations also reveal that high aspect ratio protrusions are subject to Rayleigh instability due to the temperature rise caused by field electron emission currents. As a result a large fraction of the protrusion can break off.

The model also allows for the study of the trajectories of field evaporated ions from a surface, as they are accelerated in the electric field. From the simulations we see that even changes in the surface morphology on the atomic scale may result in aberrations in atom probe tomography experiments.

Contents

List of variables

Unless otherwise stated, SI-units are used in all equations presented in this thesis. Vector quantities are in boldface.

C_V	volumetric heat capacity
$\boldsymbol{E}$	electric field
$\boldsymbol{f}_\mathrm{C}$	Coulomb force
$\boldsymbol{f}_\mathrm{L}$	Lorentz force
$\boldsymbol{F}$	local electric field
F_ev	Evaporation threshold-field
H	ionisation energy
I	current
J	current density
q	charge
Q	activation energy
$\boldsymbol{r}$	position
$\boldsymbol{r}_{ij}$	distance between ith and jth atom
$\hat{\boldsymbol{r}}_{ij}$	unit vector in directon of $\boldsymbol{r}_{ij}$
T	temperature
β	field enhancement factor
Δt	MD timestep
Φ	electrostatic potential
ϕ	work function
κ	thermal conductivity
Λ	binding energy
ϱ	charge density
ρ	resistivity
σ	surface charge density

Chapter 1

Introduction

The presence of high electric fields, of the order 100 MV/m or higher, is becoming increasingly common, as science and engineering contiunue to push boundaries. These kind of fields can be found in *e.g.* future *particle accelerators* [1, 2], *field emission microscopes* [3], *field ion microscopes* [4, 5] and *atom probes* [6–8].

Such high fields can lead to many undesired effects, such as fracturing [9–11],"dark" *field electron emission* currents from flat surfaces which can result in vacuum contamination [12] and heating [13], and *electrical breakdowns* in vacuum, which can severly damage or limit the performance of accelerators [2] and fusion reactors [14]. As an example, the future particle accelerator CLIC (Compact LInear Collider), planned at CERN, will have a length of nearly 50 km to keep the breakdown rate at an acceptable level [1]. To increase efficiency and prevent such damage it is necessary to gain insight into the processes occuring when a high electric field is applied to a surface.

It has been observed that field emission often occurs prior to breakdown [14, 15], but the exact nature of the relationship is not known. A common model is that *field emitters*, sites where there is a high degree of field emission, melt or explode, and, thereby, supply enough neutral atoms via field evaporation to enable plasma build-up and arcing [14]. It is strongly believed that these emitters are geometrical in nature, consisting of sharp features on a surface, where the applied electric field is enhanced enough to trigger field emission. These emitters can be found even on surfaces that have received special surface treatment to render them as smooth as possible [16, 17]. In some cases is has been observed that foreign particles or scratches act as emitters [16], but in many cases their origin remains unknown. By measuring the field emission current, it is possible to determine the expected shape of the emitters [18]. These measurements suggest that the emitters must have a high aspect ratio in the range $30 - 100$ [16–18], but

emitters of that kind have not been observed visually. It is, however, not possible to rule out the possibility of these kind of protrusion existing, since it may be the case that they appear when a high electric field is applied [19], and disappear when the field is removed.

Computer simulations may reveal more details that are unavailable via conventional experiments. As the electric field strength is increased the effect of individual atoms become more important. With computational methods it is possible to observe processes on the atomic level, which are experimentally inaccessible. Thus, simulations may provide the missing key information needed to fully understand the effects of high electric fields. Having such a model will help to understand exactly how a surface behaves under a high electric field, and how its properties are modified by the field. However, current atomistic simulation codes do not provide all the necessary features to be able to simulate these effects efficiently and accurately. This work aims to rectify the situation by describing an extension to classical *molecular dynamics* [20] to include electronic effects, such as induced surface charge and electrostatic forces due to an applied electric field, and resistive heating due to field emission. While the presented model is only applicable to metal surfaces, this does not present a large problem, as most of the effects described above are only relevant for conductors.

To prove the versatility of the method, the implementation is not only used to investigate the processes leading up to electrical breakdowns, but is also used to investigate *trajectory abberations* [21] in atom probe tomography (APT). APT relies on the controlled evaporation of ions from a sample under a high electric field, in such a way that the trajectories of the ions can be deduced later. A lacking understaning of these aberrations is currently a limiting factor for APT resolution, which could, in theory, reach atomic precision [22].

Chapter 2

Purpose and structure

The purpose of this thesis is to describe a new method of simulating the effects of high electric fields on metal surfaces, based on the PARCAS molecular dynamics code [23, 24], and to show how this technique can be used to gain valuable insight in the processes occurring under these conditions.

This thesis consists of a brief summary part and six original publications, which are either published or submitted for publication in international peer-reviewed journals, presented with the permission of their publishers. The publications are referred to using boldface Roman numerals within the text.

Chapter 3 briefly describes the physics needed to understand the implementation of the simulation techniques presented in Chapter 4. Some simulation results, obtained using this new method, regarding surface morphology evolution and the effect of atomic-scale roughness on the trajectories of evaporated ions, are described in Chapter 5. Finally, some closing remarks are provided in Chapter 6.

2.1 Summary of original publications

Publication I: Atomistic modeling of metal surfaces under electric fields: Direct coupling of electric fields to a molecular dynamics algorithm
F. Djurabekova, S. Parviainen, A. Pohjonen, and K. Nordlund *Phys. Rev. E* 83, 026704 (2011)

> This paper contains an overview of the algorithms used in our hybrid electrodynamics - molecular dynamics (ED-MD) implementation. Details are given for the cal-

culation of the electric field shape above a metal surface and the induced charge on the surface. The paper also contains an investigation of the accuracy of the model by comparing it with both experimental and analytical results, showing good agreement.

Publication II: Electronic processes in molecular dynamics simulations of nanoscale metal tips under electric fields

S. Parviainen, F. Djurabekova, H. Timko, K. Nordlund *Computational Materials Science* 50, 2075 (2011)

An extension to our original ED-MD model is introduced to include field electron emission and the resulting resistive heating, as well as electronic heat conduction, and compared against analytical results. Rayleigh instability can be seen in protrusions that are heated by field emission. The impact of finite size effects (FSE) is also discussed.

Publication III: Molecular dynamics simulations of nanoscale metal tips under electric fields

S. Parviainen, F. Djurabekova, A. Pohjonen, K. Nordlund *Nuclear Instruments and Methods in Physics Research Section B* 269, 1748 (2011)

The paper provides an overview of the improved ED-MD model, and shows some results regarding the impact of temperature on field evaporation from a surface protrusion. Possible formation mechanisms for such protrusions are also investigated.

Publication IV: Concurrent Electrodynamics - Molecular Dynamics - Monte Carlo simulations of field assisted evaporation in atom probe tomography

S. Parviainen, F. Djurabekova, S. P. Fitzgerald, A. Ruzibaev, K. Nordlund, Submitted for publication in *Ultramicroscopy*

The ED-MD model is further improved by describing the implementation of a Monte Carlo based step which enables simulation of field evaporation at cryogenic temperatures, when the evaporation probability of a surface atom is low. The new method is then used to investigate aberrations in trajectories of evaporated ions, caused by local changes in the electric field. Four different systems are investigated: a flat Cu

surface, a Cu surface with a pit, and a Cu surface with an Fe inclusion and a conical Cu sample similar to those used in atom probe tomography (APT) experiments. The results show that aberrations are present in all systems.

Publication V: Dislocation nucleation on a near surface void leading to surface protrusion growth under an external electric field

A. S. Pohjonen, S. Parviainen, T. Muranaka and F. Djurabekova *J. Appl. Phys.* 114, 033519 (2013)

In the presence of a near-surface void, surface protrusions may start growing when a high electric field is applied to an initially flat surface. The paper discusses the dislocation based formation mechanism and provides a detailed analysis of the stresses present in the system. The simulations show that field enhancement at the growth site leads to a positive feedback loop with catastrophic growth.

Publication VI: Molecular Dynamics Simulations of Ion Irradiation of a Surface under an Electric Field

S. Parviainen, F. Djurabekova, *Nuclear Instruments and Methods in Physics Research Section B*, in press

The sputtering yield of a material may be enhanced significantly in the presence of a high electric field. When an ion with sufficient energy impacts on a surface, the resulting change in the surface morphology results in field enhancement which, in turn, enables field evaporation of surface atoms. The sputtering yield of small surface protrusions is also investigated, and found to be significantly higher than for a flat surface. Additionally, distortion of the electric field surrounding a protrusion will lead to an increased local fluence at that site.

2.2 Author's own contributions

The author contributed a significant part to the implementation of the multigrid algorithm used in Publication **I**, as well as carried out simulations to determine the performance and accuracy of the algorithm and the screening factor used in the Coulomb interaction. The author implemented the electronic effects described in Publications **II-III**, carried out all the

simulations and analysis, except those regarding stress calculation and protrusion growth in Publication **III**, and wrote the majority of the publications. For publication **IV** the author wrote the publication in its entirety, implemented all the described additions to the ED-MD algorithm, including the concurrent Monte Carlo step and the ion trajectory calculation, as well as performed the analysis presented in the paper. For publication **V** the author of this thesis carried out the concurrent electrodynamics - molecular dynamics simulations described in the paper, as well as the analysis related to that simulation. Additionally, the author contributed by writing the description of the ED-MD algorithm and the results of the ED-MD simulation. The author wrote publication **VI** in its entirety, carried out all simulations as well as performed all the analysis presented therein.

Chapter 3

Interactions between electric fields and metals

3.1 Properties of metals

The vast majority of the elements are metallic. Defining characteristics of metals are that they have a crystalline structure while solid, they are usually ductile and malleable (meaning they can be deformed without breaking them), and they possess high electric and thermal conductivity [25]. These properties can all be explained by the electronic structure of metals. In metals the valence band and the conduction band overlap, resulting in electrons freely moving around in the metal. Thus, electrons are delocalised in an *"electron sea"*, where they interact with the positively charged nuclei to form metallic bonds [26]. Because of the delocalised nature of the bonds, atoms can slide past each other without strong repulsive forces, which explains the ductility of metals [27]. The free electrons are easily excited by photons, resulting in the shiny appearance of metals [28].

The highly mobile nature of the free electrons in metals result in a high electric conductivity, especially in metals with a high number of valence electrons, since it enables the rapid motion of a many charge carriers when an electric field is applied [29]. The relatively free motion of the electrons also contribute to the thermal conductivity of metals. When a metal is heated, the kinetic energy of both electrons and nuclei is increased. Because the mobility of the lightweight electrons is much greater than that of the heavier nuclei, the electrons contribute significantly more to the transport of thermal energy in metals. Thus, the thermal conductivity of a metal is almost completely electronic in nature, while the heat conduction via lattice vibrations only accounts for some per cents [29].

3.2 Surface charge induced by an electric field

When an electric field is applied to a metal surface, it affects the free electrons in the metal, restricting their motion by either pulling them towards the surface, or pushing them away from the surface, leading to either an excess or a depletion on the surface. Thus, the surface receives a net electric charge, which can be calculated by Gauss' Law using the "pill box" technique [30]

$$\sigma(\boldsymbol{r}) = \varepsilon_0 E(\boldsymbol{r}), \tag{3.1}$$

where $\sigma(\boldsymbol{r})$ is the surface charge density at a point $\boldsymbol{r}$, ε_0 is the permittivity and $E(\boldsymbol{r})$ is the absolute value of the electric field strength at the same point r on the surface. The induced charge appears as a modification to the electron density around the surface atoms [31], giving the atoms an "effective" fractional charge (*i.e.* does not need to be a multiple of the unit charge), ignoring polarisation effects. If the metal does not form a circuit it will eventually reach electrostatic equilibrium and the induced surface electric charge on both surfaces will cancel out any internal electric field beneath a certain skin depth which depends on the rate of change in the electric field (2 Å for a static field [30]).

Charged surface atoms will interact with each other via the Coulomb interaction. However, because of the free electrons in the metal, the charge of each atom is heavily screened [26], and the range of the interaction remains limited. Thus, the Coulomb force between two atoms i and j on the surface can be written as

$$\boldsymbol{f}_{\mathrm{C}} = \frac{1}{4\pi\varepsilon_0}\frac{q_i q_j}{r_{ij}^2}\hat{\boldsymbol{r}}_{ij}\exp(-\xi r_{ij}), \tag{3.2}$$

where q_i and q_j are the effective charges of atoms i and j, $\boldsymbol{r}_{ij}$ the distance between the two atoms, $\hat{\boldsymbol{r}}_{ij}$ the unit vector in the direction of $\boldsymbol{r}_{ij}$ and ξ a material and surface orientation dependent screening factor. For *e.g.* the Cu $\{100\}$ surface this limits the interaction to ≈ 3 Å. The interaction is, thus, essentially limited to nearest or next-nearest neighbour atoms, and the effect remains quite limited.

3.3 Impact of surface geometry on the shape of an electric field

The shape of the electric field above a metal surface is affected by the shape of the surface itself. Due to geometric effects the electric field can be heavily distorted around features such as surface asperities.

The electric field can be defined as the gradient of the electrostatic potential $\Phi(\boldsymbol{r})$, which in turn, for metals, is given by Poisson's equation [30]

$$\boldsymbol{\nabla}^2\Phi(\boldsymbol{r}) = -\frac{\varrho(\boldsymbol{r})}{\varepsilon_0}, \tag{3.3}$$

where $\varrho(\boldsymbol{r})$ is the charge density.

In the specific case of a conducting surface at equilibrium, the entire surface is, by definition, at the same potential. Thus, a constant value (*Dirichlet*) boundary condition should be used at the surface when solving Eq. (3.3) in the case of a metal. On the other hand, the local surface shape should not affect the shape of the electric field at sufficiently large distances. Thus, *e.g.* in the case of a flat surface, the electric field should have a set value at infinity, *i.e.* a *Neumann boundary* is required.

If it is assumed that there are no free charges such as ions or electrons above the surface,*i.e.* $\varrho(\boldsymbol{r}) = 0$, Eq. (3.3) simplifies to Laplace's equation

$$\boldsymbol{\nabla}^2\Phi(\boldsymbol{r}) = 0. \tag{3.4}$$

It is often useful to make this kind of approximation, as it results in a simpler treatment, and is usually easier to solve than Eq. (3.3). While it is possible to solve these equations analytically in simple cases [30], in the general case a numeric solution is required.

3.3.1 Field enhancement

As a result of the geometric effects mentioned above, the electric field is strengthened at sharp features, where electric field lines converge, while it is weakened elsewhere (Fig. 3.1).

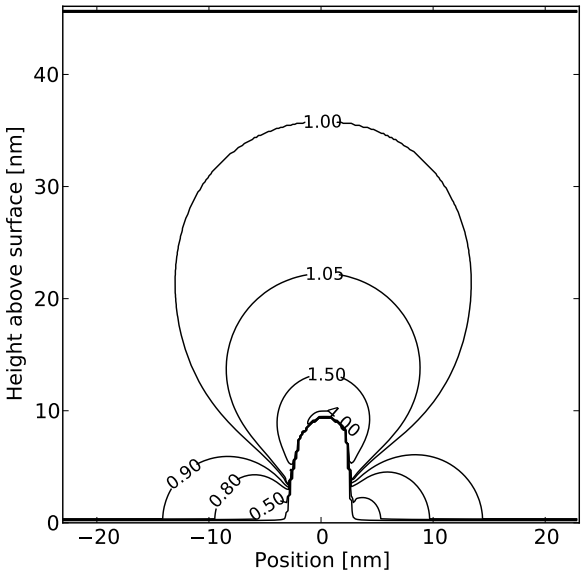

Figure 3.1: Shape of the electric field around a protrusion. The lines show the field enhancement, *i.e.* the local field strength compared with the applied field. It is seen that the field is enhanced directly above the protrusion, while it is weakened at the base.

The ratio of the local electric field immediately above a surface, $\boldsymbol{F}$, and the applied field $\boldsymbol{E}$, *i.e.* the field in the absence of any geometric features, is known as the *field enhancement factor* often denoted β. Thus, the local electric field at a surface is given by

$$\boldsymbol{F} = \beta \boldsymbol{E}. \tag{3.5}$$

In many cases it is not necessary to know the exact field shape, but rather only the strength of the local electric field. Simple approximations exist for a variety of simple geometrical shapes, such as hemispheres, hemiellipsoids and cylinders on metal surfaces [30, 32–34]. For a surface feature of the shape of a hemispherical cap on top of a cylinder, the field enhancement factor is given with high accuracy by [35]

$$\beta \approx 1.2 \left(2.15 + \frac{h}{r}\right)^{0.90}, \tag{3.6}$$

where h and r is the height and radius of the cylinder. This kind of simple structure is often used to approximate *field emitters* [2, 32], described in Chapter 3.4. The less accurate, but much simpler, equation

$$\beta \approx \frac{h}{r} + 3 \approx \frac{h}{r}, \tag{3.7}$$

can be employed when $h/r < 100$ [32].

Field enhancement can further be increased by having multiple geometric shapes stacked on top of each other [34]. In this case, the field is first enhanced by the lower structure by a factor β_1, after which is further enhanced by the higher structure by a factor β_2 resulting in a total enhancement factor of $\beta = \beta_1\beta_2$. Thus, while surface roughness alone, resulting in a relatively modest enhancement [36] $\beta_{\text{rough}} \approx 2$, does not cause the local field to be strengthened significantly, it does reduce the needed aspect ratio of smaller features to obtain very high fields.

3.4 Field electron emission

In the free electron model, electrons are free to move around inside bulk material, but to escape from the surface they must overcome an energy barrier. The height of the barrier, compared with the Fermi level E_{F}, is known as the *work function* [26] ϕ. Electrons can obtain the energy necessary to overcome this barrier from *e.g.* heating (*thermionic emission*, discovered in 1873 and explained by Richardson in 1901 [37]), photons (*photoinduced emission*, discovered in 1887 and explained by Einstein in 1905 [38]) or other radiation (*e.g. secondary electron emission*). The electrons can also tunnel through the energy barrier, especially when an external electric field is applied (*field emission*, discovered in 1922 and explained by Fowler and Nordheim in 1928 [39]).

An electron gains energy when it moves in the direction of a negative electric field and the further away from the surface the electron moves the more energy it will obtain. Thus, in the presence of such a field, the escape barrier will have a finite width and decrease with distance. If the barrier width is reduced sufficiently, electrons may tunnel through the barrier [40]. Additionally, the escaping electron will induce an image charge below the surface, lowering the height of the escape barrier [41] (Fig. 3.2). The lowered barrier height will also lead to increased thermal emission, as some electrons will statistically have enough energy to overcome the lowered barrier [42].

The field emission tunnelling current is given by the Fowler-Nordheim equation [41]

$$J(F, T, \phi) = \lambda_{\text{T}}(T)\frac{aF^2}{\phi}\exp\left(-\frac{\nu(F)b\phi^{3/2}}{F}\right), \tag{3.8}$$

where ϕ is the material and orientation dependent surface work function, F the local electric field, a and b are constants, $\nu(F)$ is a correction factor to describe the barrier shape and $\lambda_{\text{T}}(T)$ is an approximate temperature dependent correction factor.

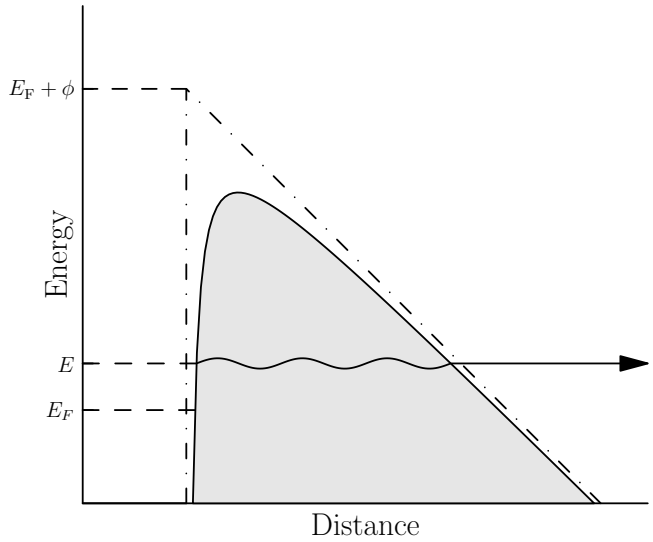

Figure 3.2: Schematic illustration of the barrier an electron, with energy E, has to overcome in order to escape a surface. At high fields the barrier width will be reduced sufficiently to enable electrons to tunnel through the barrier. The dashed line corresponds to a simple barrier where the image charge is not accounted for.

Despite the temperature dependent correction, the FN-equation is only valid in a limited domain at low temperatures and high fields [42] because of the approximations used when deriving it. Eq. (3.8) also breaks down at very high fields as the tunnelling probability approaches unity (Fig. 3.3). While more advanced models of electron emission exist [42–44], they have not been tested as thoroughly as the simple Fowler-Nordheim model and are, therefore, not considered further here.

Once a substantial amount of electrons have been emitted, they may start to screen the external electric field, limiting the electron current [45, 46]. This effect is known as *space-charge screening*, and may play a large role when the emission current density is sufficiently high and the gap between electrodes is small. However, this effect is negligible at the onset of emission [47], as it takes time to build up enough charge in the space above the emitter.

3.5 Resistive heating due to field emission

When an electric current flows through a material, it will result in an increased temperature, as energy from the moving charge carriers is transferred to atoms in the material via collisions. Thus, it is necessary to consider the temperature rise in a field emitter when the field strength is significant enough to cause high density field emission currents.

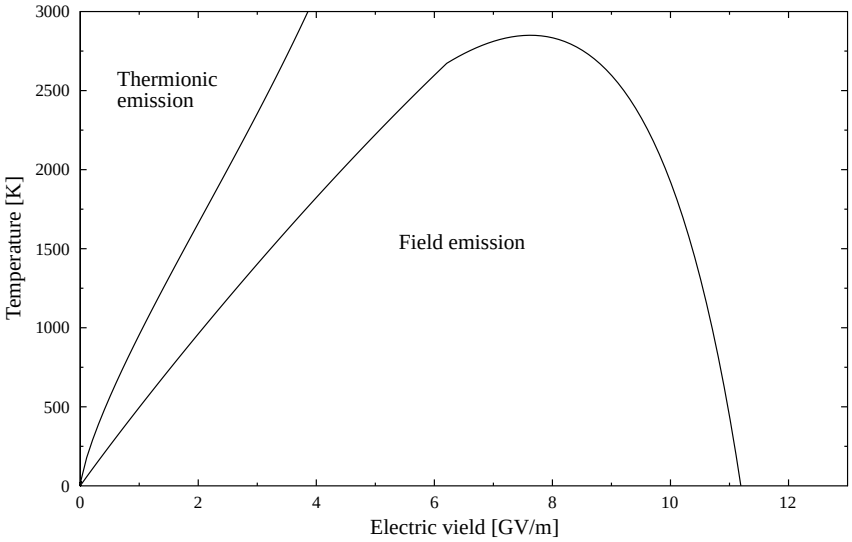

Figure 3.3: Thermal- and field emission regions for a metal with work function $\phi = 4.5$ eV (*e.g.* Cu). Electron emission in the thermionic region is described by the Richardson equation [37], while emission at low temperature and high fields is described by the Fowler-Nordheim equation (Eq. (3.8)). Neither equation describes emission at high fields and high temperatures, or very high fields.

The temperature, T, at point $\boldsymbol{r}$ and time t of a system being heated by an electric current is given by the heat equation

$$\frac{\partial T(\boldsymbol{r},t)}{\partial t} = \frac{\kappa(T)}{C_{\mathrm{V}}}\nabla T(\boldsymbol{r},t) + \frac{1}{C_{\mathrm{V}}}\rho(T)J(\boldsymbol{r},T)^2, \tag{3.9}$$

where κ is the thermal conductivity of the system, C_V the volumetric heat capacity, ρ is the electric resistivity of the material and J is the electric current density.

For metals, the resistivity increases with temperature, since the increased random motion of atoms in the material results in more collisions between the atoms and the electrons in the electric current. This effect can modify the resistivity by more than an order of magnitude when comparing resistivity at room temperature and near the melting point. While the temperature effect on resistivity is often approximated as a linear dependence, in reality the situation is slightly more complex, with the resistivity often being super-linear at low temperatures due to *e.g.* the increased relative importance of intrinsic resistivity.

Another, in some cases even more important factor that has to be considered, are *finite size effects* (FSE). In addition to colliding with atoms, electrons may also scatter from surfaces, if they do not possess sufficient energy to penetrate them. For small features, of the size of the electron mean free path or smaller, the probability of surface scattering increases significantly, because

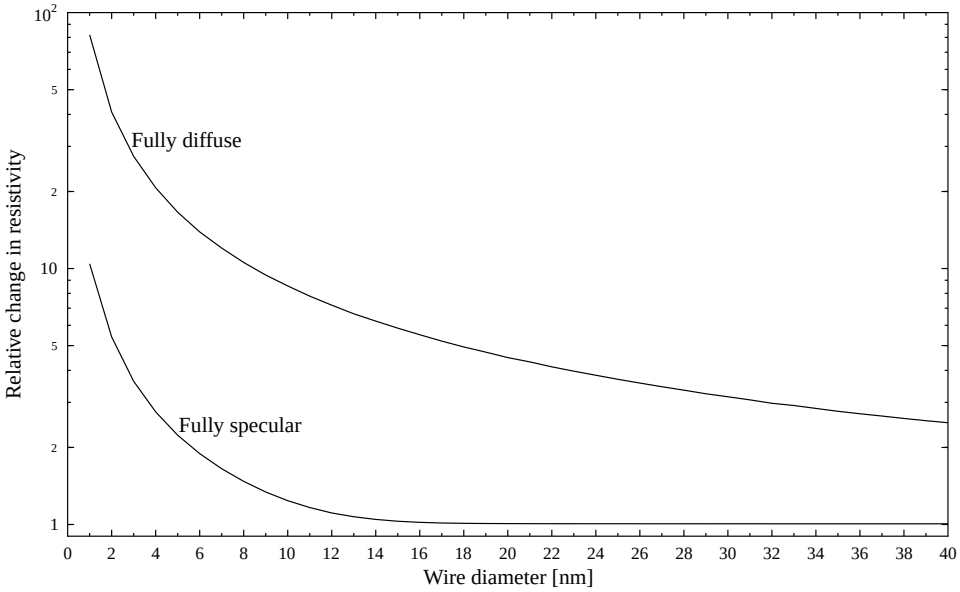

Figure 3.4: The resistivity of a nanowire relative to the bulk resistivity in Cu assuming fully specular or diffuse electron scattering at boundaries, as given by the simulation code desribed in Ref. [50].

electrons are always located within a short distance from a surface. This effect increases with decreasing feature size, and, thus, for nanosized field emitters, the resistivity may be increased by orders of magnitude (Fig. 3.4), leading to much faster heating. The electron reflection may be either specular or diffuse, depending on the surface roughness and electron wavelength. For surface roughness $R_a > 1$ nm, electron scattering is almost exclusively diffuse [48, 49].

Both temperature and FSE also affect the thermal conductivity, since its roots also lie in the motion of electrons. Indeed, for metals the relationship between the two is linear at over a wide temperature range, except in the range $T \approx 10-200$ K, assuming electrons are mostly scattered elastically [26]. Thus, heat transport is reduced in small features, leading to less effective cooling of hot field emitters, further increasing the temperature they may reach with a given current flowing through them.

In addition to resistive heating, the temperature of a protrusion will also be affected by the *Nottingham effect* [51, 52]. Electrons leaving the protrusion will, on average have a different temperature than the electrons replacing them. This effect is, however, negligable compared with resistive heating when changes in resistivity due to FSE are considered.

3.6 Field assisted evaporation of surface atoms

As stated in Chapter 3.2 when an electric field is applied to a surface it will induce a surface charge. The charged atoms will, in turn, interact with the field, and will be pulled in the direction of the field by the Lorentz force

$$\boldsymbol{f}_{\mathrm{L}} = q\boldsymbol{E}, \tag{3.10}$$

where q is the charge of the atom and $\boldsymbol{E}$ the electric field at the same point. If the applied field is of sufficient strength, the force acting on the charge at the atom becomes stronger than the force which binds the atom to the surface, thus, causing the atom to be released from the surface. At this time, there is a high probability that the atom is ionised, due to energetics [53].

It is, however, also known that neutral atoms may evaporate from the surface [54], especially in the case of a cathode. When a negative field is applied, it is possible for these evaporated neutral atoms to be ionised by the electron current, so that they obtain a positive charge [47]. These electric charges can then be accelerated by the applied electric field towards the same surface they initially evaporated from, resulting in sputtering, *i.e.* further neutral atoms being kicked out from the surface by the incident ion [55]. This cycle of released neutrals being ionised and causing further release of neutrals contribute to the build up of plasma and vacuum arcing [14], with potentially devastating effects. The number of ejected atoms per incident ion is known as the *sputtering yield*, and depends on the energy of the ion [56, 57]. Fast ions have enough energy to eject a large number of atoms. However, if the energy is high enough the ion will simply penetrate deep below the surface, depositing limited energy at the surface, and little sputtering occurs [58].

The evaporation of atoms from a surface can either be *thermally activated*, or the result of quantum mechanical *ion tunnelling* [53, 54]. However, tunnelling only has a significant effect for light elements and at very low temperatures [54, 59]. Therefore, only thermally activated evaporation needs to be considered in most situations, which is also the case of this thesis.

The exact mechanism for field evaporation is not currently known. However, two main models have been proposed for the evaporation of charged ions: the *image hump model* by Müller [60], where it is assumed that an atom is evaporated fully ionised, and the *charge drain model* by Gomer [61] where it is assumed that an evaporated atom is charged as it moves further away from the surface. While the latter model seems to be more physically motivated [53], the model by Müller, nevertheless, seems to describe the energetics of evaporation correctly [59] while

simultaneously being a conceptually simpler model. For this reason, the image hump model is used here.

In the thermally activated regime, the evaporation probability of an ion of type α and n-fold ionisation is given by the Arrhenius-type equation [59]

$$P = A \exp(-Q_{\alpha,n}(F)/k_{\mathrm{B}}T), \tag{3.11}$$

where A is a constant prefactor, $Q_{\alpha,n}(F)$ is the activation energy of the evaporation process, k_B is the Boltzmann constant and T is the temperature at the surface.

The evaporation activation energy is given by [59]

$$Q_i = \delta_i^{1/2} + \frac{1}{2}(1-\delta_i)\ln\left((1-\delta_i^{1/2})(1+\delta_i^{1/2})^{-1}\right) K_i, \tag{3.12}$$

where

$$\delta_i = 1 - F/F_{\mathrm{ev}} \tag{3.13}$$

is the fractional field deficiency and F_{ev} is known as the critical evaporation field, at which the activation energy is reduced to zero.

The critical evaporation field can be approximated using Müller's evaporation-field formula [60]

$$F_{\mathrm{ev}} = \frac{4\pi\varepsilon_0}{ne^3} K_i^2, \tag{3.14}$$

where

$$K_i = \Lambda_i + H_{n,\alpha} - n\phi_\alpha \tag{3.15}$$

and Λ_i, $H_{n,\alpha}$ and ϕ_α are the binding energy, energy required for n-fold ionisation and work function, respectively.

Chapter 4

Implementation of electronic effects in molecular dynamics

4.1 Classical Molecular Dynamics

Molecular Dynamics (MD) is a simulation method developed in the late 1950s [62] where the trajectories of individual particles, or even planets, are calculated by solving Newton's equation of motion. A simplified description of the MD algorithm for atomistic simulations is given in Fig. 4.1. First an initial atomic configuration is given as user input. The atoms may be given an initial temperature by giving them an initial velocity generated from the Maxwell distribution. Then, the atomic trajectories are calculated iteratively by repeatedly determining all forces acting on each atom, and then solving Newton's equation of motion by employing a numerical integration algorithm such as velocity Verlet [63] or Gear5 [64].

Classical MD is based on the *Born-Oppenheimer approximation* [65], which states that electrons surrounding a nucleus move so much faster than the nucleus itself, that the electrons will (on the timescales used in MD) reach equilibrium instantaneously regardless of the motion of the atoms. Thus, the electrons can be treated as always being in the ground state.

The length of the timestep, Δt, depends on the maximum velocity of the atoms in the system. If the timestep used in the integration scheme is too large, the system will behave unphysically, *e.g.* the total energy will not be conserved. On the other hand, to maximise performance, the timestep should not be smaller than necessary, due to diminishing returns. In the case where the system temperature does not change significantly, a constant timestep can be employed, based on the maximum expected velocity of any atom.

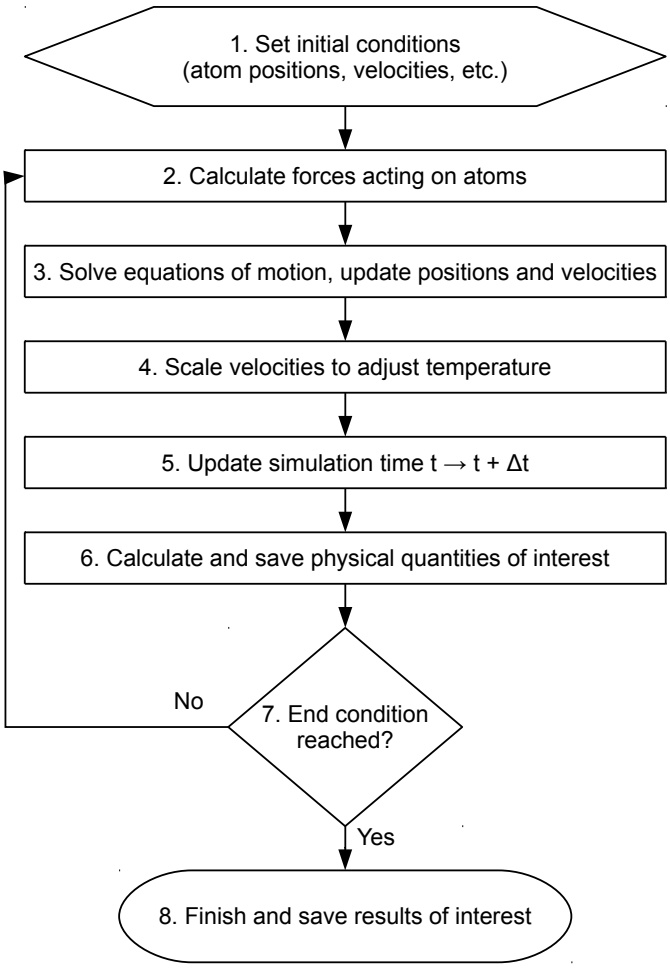

Figure 4.1: The basic steps in the molecular dynamics algorithm

To maximise efficiency, a variable timestep can be used in non-equilibrium simulations [66]

$$\Delta t = \min\left(a\frac{k_t}{v_{\max}}, \frac{E_t}{F v_{\max}}, 1.1\Delta t, \Delta t_{\max}\right), \tag{4.1}$$

where k_t and E_t proportionality constants, v_max the maximum velocity of any atom in the system, and $\Delta t_{\max}$ the maximum allowed timestep. Using this scheme the timestep length is allowed to change only 10% each step to prevent sudden changes.

The above mentioned MD algorithm is used to simulate a micro-canonical ensemble, where the total energy is conserved [20]. However, to initially equilibriate the system, or to remove excess energy introduced to the system via *e.g.* ion irradiation or resistive heating, the algorithm can be modified to include a thermostat.

An example of such a mechanism is the Berendsen thermostat [67] which works by scaling atomic velocities by the factor

$$\lambda_{\mathrm{B}} = \sqrt{1 + \frac{\Delta t}{\tau_{\mathrm{T}}} \left(\frac{T_0}{T} - 1 \right)}, \tag{4.2}$$

where τ_{T} is a user defined constant determining the efficiency of the temperature control, T_0 is the desired system temperature and T is the current system temperature. The constant τ_{T} should be chosen so that it is small enough that the expected cooling occurs, while it has to be large enough to allow for natural oscillations in the system temperature. The scaling can be applied either to the full system, or just at the borders of the simulation cell. While the Berendsen thermostat, unlike some other thermostats [68–70], does not result in a canonical ensemble, it is, nevertheless, useful as it is efficient while at the same time retaining reasonable accuracy.

Because molecular dynamics is computationally expensive it can only be used with systems of a limited size. Very large systems can be approximated by an infinite lattice by using *periodic boundary conditions* (PBC). When an atom moves across a border in the simulation cell it reappears at the opposite side, and all interactions also wrap around edges. Self-interaction may become an issue if the simulated system is too small, *e.g.* defects start interacting with themselves through strain fields in the cell [20]. When simulating large surfaces it is possible to use periodic boundaries only perpendicular to the surface, while using an open boundary along the surface normal. In this case it is also possible to prevent self-interaction by restricting the motion of atoms at the periodic boundaries to only move in the direction of the surface normal.

The MD code used for this study is based on PARCAS [23, 24]. In all simulations either restricted PBC (publication **V**) or normal PBC (all other publications) were used perpendicular to the surface normal, while atoms at the bottom were fixed. A fixed timestep was used in all simulations except the ones presented in **VI** which used an adaptive step as presented above.

4.1.1 Inter-atomic potentials

The Embedded Atom Method (EAM) is a suitable formalism to describe the interatomic potential for most metallic systems [71]. This formalism is based on the "electron sea" model of delocalised electrons, and considers the energy required to embed an atom into this electron system.

In EAM the potential energy of atom i is given by

$$E_i = F_i\left(\sum \rho_j(\boldsymbol{r}_{ij})\right) + \frac{1}{2}\sum V_{ij}(\boldsymbol{r}_{ij}), \tag{4.3}$$

where F_i is the energy required to embed the atom into the electron sea, ρ_j is the contribution to the electron density from atom j, r_{ij} is the distance between atoms i and j and V_{ij} a pair potential interaction. The functions ρ and V are material dependent and determined by *e.g.* fitting to experimental or *ab initio* results. Because the range of the interaction is limited, and because number of particles is usually very high in atomistic simulations, usually only the contribution of the nearest neighbours or the next-nearest neighbours j are included in the energy calculation. Additionally, a neighbour list may be used to further speed up computation.

The potentials used in the publications included in this thesis are the Sabochick-Lam [72] and Mishin [73] potentials for pure Cu systems and the Malerba-Pasianot [74] potential for mixed Cu-Fe systems which is based on the Mishin and Mendelev [75] potentials. The Sabochick-Lam potential is designed to reproduce radiation induced amorphisation while the Mishin potential is designed to accurately reproduce the energetic for non-equilibrium structures such as in the presence of various extended defects. The Mendelev potential for Fe is designed to describe liquid Fe well, but also gives *e.g.* good results for the energetics of defects. As a combination of the previous two potentials, the Malerba-Pasianot potential also share many of their favourable properties.

4.2 Concurrent electrodynamics - molecular dynamics

4.2.1 Motivation

Classical molecular dynamics does not normally account for dynamical electronic effects. While some MD codes include electrostatic interactions between atoms [76, 77], the charge state of individual atoms must often be provided as user input. Additionally, most such codes are designed for use with molecules, and are, therefore, not suitable for handling large metallic systems.

As mentioned in Chapter 3.1 electronic heat conduction is the dominant form of transport for thermal energy in metals. However, as it is electronic in nature, classical molecular dynamics is unable to account for it. In non-equilibrium simulations *electron-phonon coupling* (EPC) [78, 79] has been used to simulate cooling due to electronic effects. EPC is, however, not suitable for

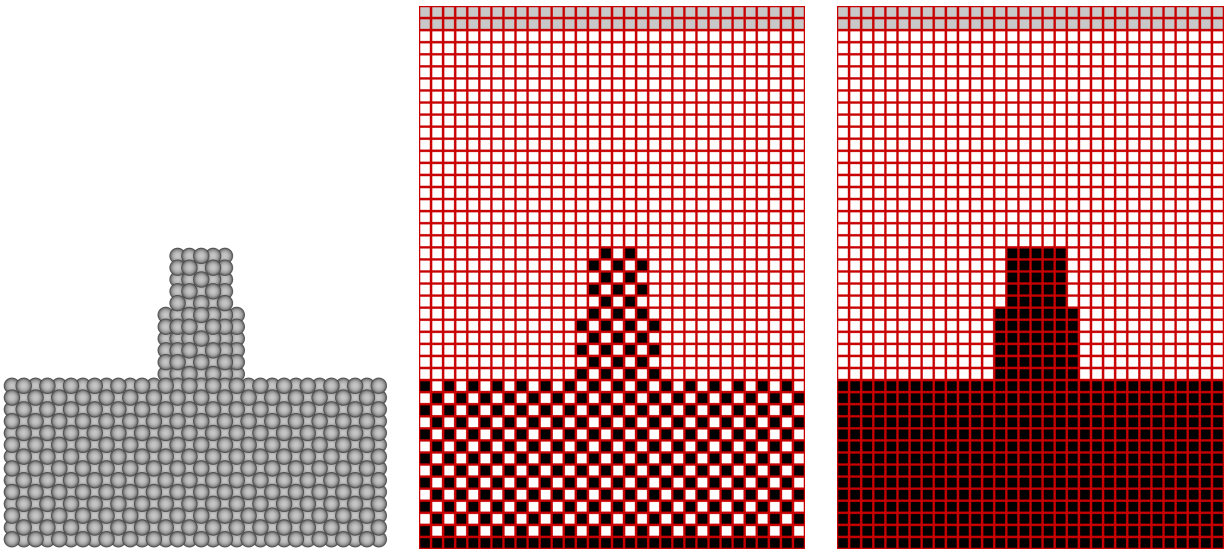

(a) (b) (c)

Figure 4.2: Example of a simulated system (a). The atomic system is constructed by assigning each atom to a gridpoint (b). Gaps are then filled to simulate a continuous system (c). Images b) and c) only show a 2D slice of the system for clarity.

near-equilibrium simulations, and, additionally, fails to account for geometrical effects, and is, therefore, generally only valid for bulk simulations.

This chapter contains a brief overview of the implementation of electronic effects in molecular dynamics, including surface charge induced by an external electric field, additional electrostatic forces, field assisted evaporation at low temperatures, resistive heating due to field electron emission and electronic heat conduction. A detailed description of the implementation can be found in publications **I-IV**.

4.2.2 Discretisation

Many of the results in classical electrodynamics, such as Eq. (3.1) (Gauss' law) and Eq. (3.4) (Laplace's equation) were derived in a continuum limit, while the systems simulated in MD consists of individual, discrete, atoms. To rectify the discrepancy, it is possible to perform the computations on a discretised grid. Under this scheme, an atom occupies a single grid point, and the electric field is also calculated using the same grid. To emulate continuous matter, space between atoms is also considered to be "filled". Both the discrete atomic system used in MD and the continuous system used in electrodynamics are, thus, approximated using the same discretised grid (Fig. 4.2), eliminating the discrepancies between the two schemes. Because the system is allowed to evolve with time, the grid is reconstructed at every MD timestep. A

limitation of this technique is that two atoms are not allowed to occupy the same grid point. However, such a situation is rare, since it is uncommon to find atoms within such proximity of each other in a solid metal system.

For the construction of the grid it is assumed that the system is crystalline. For every unit cell there are 8 grid points. Because the MD lattice spacing may change in the direction of the open surface, *e.g.* due to surface relaxation or interaction with the electric field, the grid spacing in that direction is recalculated at every MD timestep. This is accomplished by assigning each atom to an atomic layer using k-means clustering [80], and then calculating the average separation between the layers.

4.2.3 Electric field calculation

As noted in Chapter 3.3 the local shape of an electric field above a metal surface depends strongly on the shape of the surface itself. In our implementation, the value of the *electrostatic potential* at each grid point is calculated by solving Eq. (3.4) using the finite difference method [81], and the boundary conditions appropriate for conducting surfaces, *i.e.* Dirichlet boundary at the surface itself and a Neumann boundary far above it. Periodic boundaries are used elsewhere. The electric field is calculated at every MD timestep, except if the grid used for the calculation has not changed since the last time, as the calculation would give exactly the same result as at the previous timestep. The previous solution for the electric field is used as an initial guess for the solution at the next time step.

Using the central difference approximation [81]

$$\frac{\partial^2 \Phi(x)}{\partial x^2} \approx \frac{\varphi_{i-1} - 2\varphi_i + \varphi_{i+1}}{(\Delta x)^2}, \tag{4.4}$$

where φ_i is the potential at the ith gridpoint and Δx the grid spacing, Eq. (3.4) can be approximated as

$$\begin{aligned} \boldsymbol{\nabla}^2 \varphi(x,y,z) \approx & \frac{\varphi_{i-1,j,k} - 2\varphi_{i,j,k} + \varphi_{i+1,j,k}}{(\Delta x)^2} \\ & + \frac{\varphi_{i,j-1,k} - 2\varphi_{i,j,k} + \varphi_{i,j+1,k}}{(\Delta y)^2} \\ & + \frac{\varphi_{i,j,k-1} - 2\varphi_{i,j,k} + \varphi_{i,j,k+1}}{(\Delta z)^2} \\ = & 0 \end{aligned} \tag{4.5}$$

To reach a good approximation of the correct result, Eq. (4.5) must be iterated several times, using the Gauss-Seidel method [80]. Thus, the number of equations to solve may be very large for systems with numerous grid points and when many iterations are needed. To speed up computation our implementation employs the *multigrid method* [80, 82], which can increase the performance of the above calculation by many orders of magnitude (Fig. 4.3). The algorithm reduces the total number of calculations necessary by working on a coarser grid with fewer grid points, and then extrapolating the result to a finer grid (Fig. 4.4).

The algorithm can be summarized as follows:

1. Make an initial guess
2. Perform a few iterations using Eq. (4.5) to get an initial approximation
3. Restrict residual to coarser grid using the restriction operator
4. Solve correction term using calculated residual on coarser grid
    - Solve using recursion if grid can be made coarser
    - Solve using relaxation if grid cannot be made coarser
5. Interpolate correction term to finer grid using the prolongation operator
6. Apply postsmoothing
7. Iterate above steps, using previous result as initial guess

Once the potential is known at every point, the electric field is determined using the finite difference approximation.

The calculation of the electric field can be further sped up, by restricting the volume where the field is solved around a certain region of interest. For instance, if a small change to surface geometry occurs in a well-defined area, it can be assumed that the field remains unchanged far away from that point, and it is, thus, possible to simply solve the electric field in a smaller region of interest, while forcing the solution to remain unchanged at the boundaries.

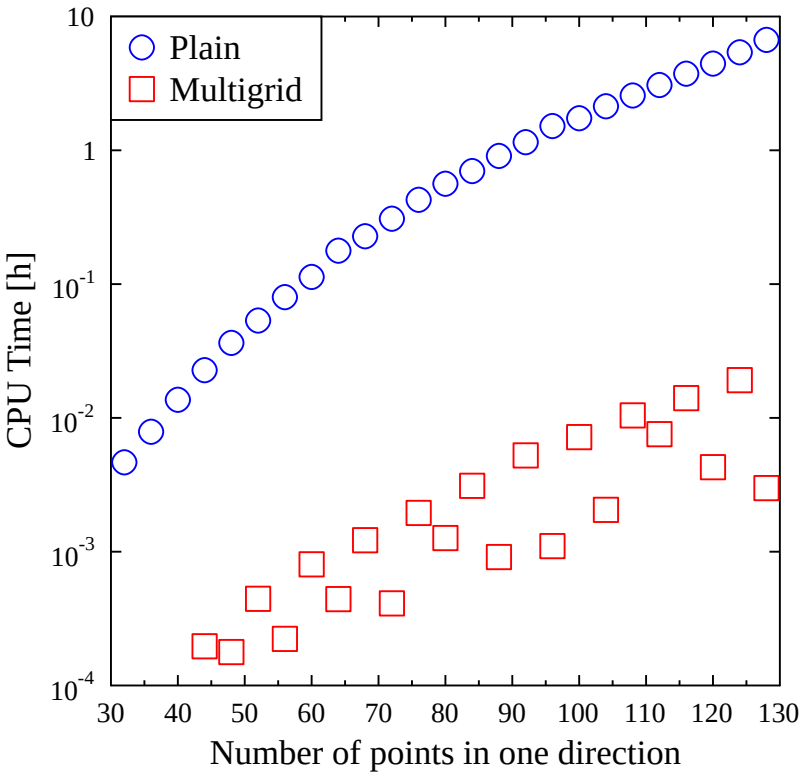

Figure 4.3: Comparison of time taken to solve electric field using plain Gauss-Seidel iteration and Gauss-Seidel iteration with the multigrid method

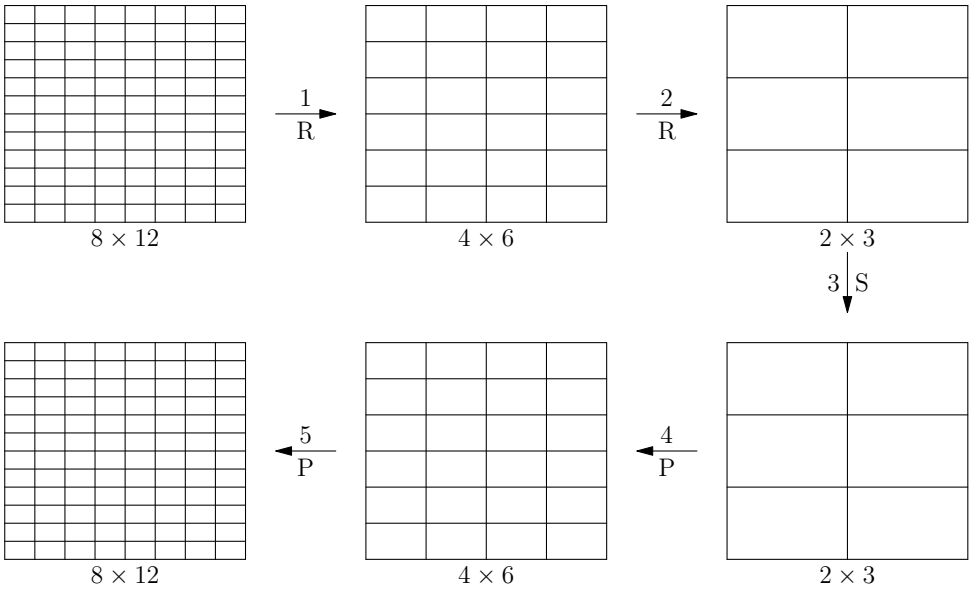

Figure 4.4: In the multigrid method an equation on the original grid is transferred to a coarser grid where it is solved and then transferred back to the original grid. Here R represents a restriction operation, S a solving operation and P a prolongation operation.

4.2.4 Charge calculation and forces

Under the influence of an external electric field, the electron density at the surface will change due to the interaction between the field and the electrons in the metal beneath the field. The change in charge is considered to be localised around the surface atoms, so that it can be considered that the surface atoms themselves become charged. The charge induced on each atom by the applied field is calculated using a discretised form of Eq. (3.1), where the electric field at each gridpoint surrounding an atom contributes a partial charge to that atom, proportional to the value of the electric field at that point, and the surface area in the direction of the field. In reality the electric field will always be perpendicular to a metal surface. However, due to the finite grid spacing used here, a parallel component may also appear. This component is unphysical, and, hence, only the component perpendicular to the surface is taken into consideration here (Fig. 4.5). The contribution of grid point i on atom j is, thus,

$$\delta q_j^i = \varepsilon_0 F^i A^j, \tag{4.6}$$

were F^i is the electric field at gridpoint i and A^j is the area of the gridpoint perpendicular to F^i.

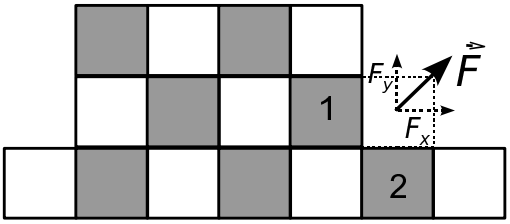

Figure 4.5: 2D projection of the discretised model illustrating force calculation. The atom at gridpoint 1 only feels the force component F_x while F_y is ignored. For the atom at site 2 the situation is reversed.

The total charge of an atom is, thus, given by

$$q_j = \sum_{i=0}^{N_j} \delta q_j^i, \tag{4.7}$$

where δq_j^i is the contribution of grid point i on atom j.

Once the surface atoms have received a charge, they will interact with each other via the Coulomb force (Eq. (3.2)) and the electric field via the Lorentz force (Eq. (3.10)), which will pull the charged atoms in the direction of the field. If the field is strong enough, it can overcome the energy barrier which binds the atom to the surface, and the atom will evaporate. In our implementation an atom is considered evaporated once no atom can be found at a neighbouring grid point. When the atom is marked as evaporated it no longer interacts with the rest of the system. All atoms evaporated in such a way are considered to be neutral. This can be justified if evaporation is simulated directly only when a negative field is applied, in which case evaporation to a neutral state is more likely [83].

4.2.5 Field emission and resistive heating

When the applied electric field is strong enough, heating by field electron emission becomes significant, especially when finite size effects are taken into account. In the current implementation, the density of the field emission current inside the emitter is first calculated, and is then used to solve Eq. (3.9) inside the emitter to determine its temperature distribution.

To obtain the density of the field emission current flowing through the emitter, the total emission current I_{tot} is first calculated by using the FN equation to calculate a partial current at each grid point at the emitter surface. It is then assumed that this current flows all the way from the bottom of the emitter through the very apex, and, thus, the current density at height x in the emitter is given by

$$J(x) = \frac{I_{\text{tot}}}{A(x)}, \tag{4.8}$$

where $A(x)$ is the cross-sectional area of the emitter at height x. The current density is, thus, larger at narrow parts of the protrusion.The velocities of affected atoms in the emitter are then scaled, so that their kinetic energy correspond to that of the calculated temperature. A Berendsen-type time constant is applied to the scaling to prevent rapid and unphysical fluctuations in the system.

For simplicity, only a 1D temperature distribution for the emitter is calculated, using the finite difference method to solve Eq. (3.9). This is justified if the emitters being studied display a high degree of symmetry. The base of the emitter is assumed to be connected to a large heat bath at constant temperature, while the top of the emitter is assumed to be thermally isolated. Because cooling by thermal radiation is many orders of magnitude lower than by conduction it can be ignored here. When solving the heat equation the temperature dependence of the resistivity is taken into account by interpolating between precomputed values based on the work of Schuster et al. [84]. The corresponding thermal conductivity is then computed using the Widemann-Franz law [26]. Finally, finite size effects are handled by scaling the obtained resistivity and thermal conduction coefficients by a constant scaling factor obtained from other simulations.

4.2.6 Field evaporation at cryogenic temperatures

At cryogenic temperatures the evaporation probability of a surface atom is low, as indicated by Eq. (3.11), which means that there is a long time between evaporation events, on an MD time scale. To, nevertheless, be able to simulate this kind of evaporation, an additional *Kinetic Monte Carlo* (KMC) [85] based step is introduced, in which surface atoms are forced to evaporate at a regular interval. This guarantees that a number amount of evaporation events occur within the limited time span accessible by MD simulations. For simplicity, only one atom is allowed to evaporate at a time, which is also a targeted condition in *e.g.* atom probe tomography (APT) [53]. The atom to evaporate is picked from a distribution based on the evaporation probabilities of all the atoms.

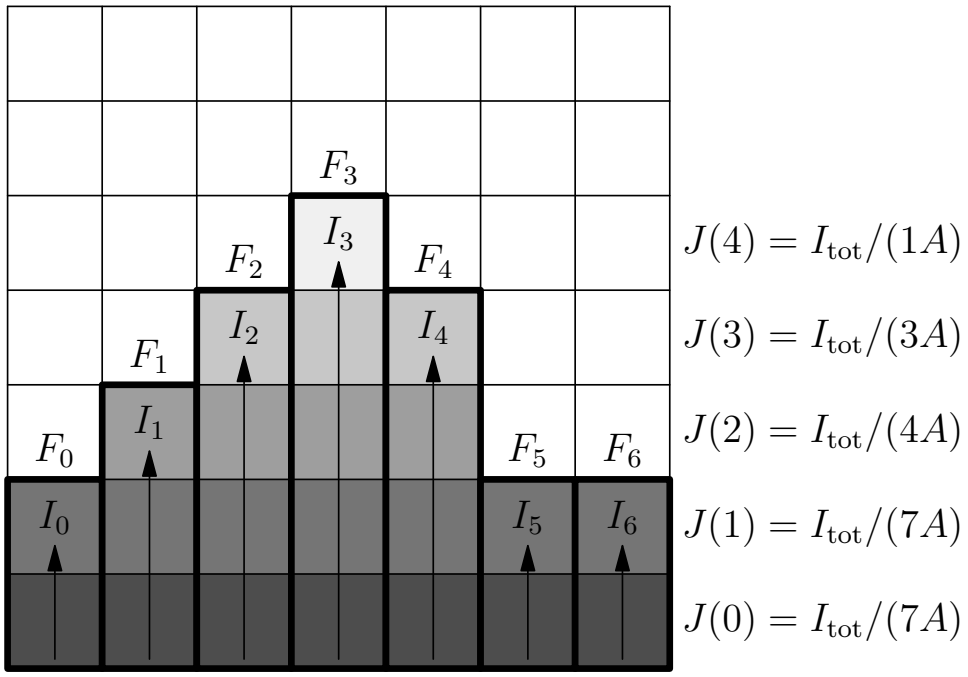

Figure 4.6: Schematic illustration of the calculated current density inside a protrusion. The total current, I_{tot}, is calculated by summing the contribution from each atomic column. The current density at a given height is then taken to be the total density divided by the cross-sectional area, A, of each column at that height.

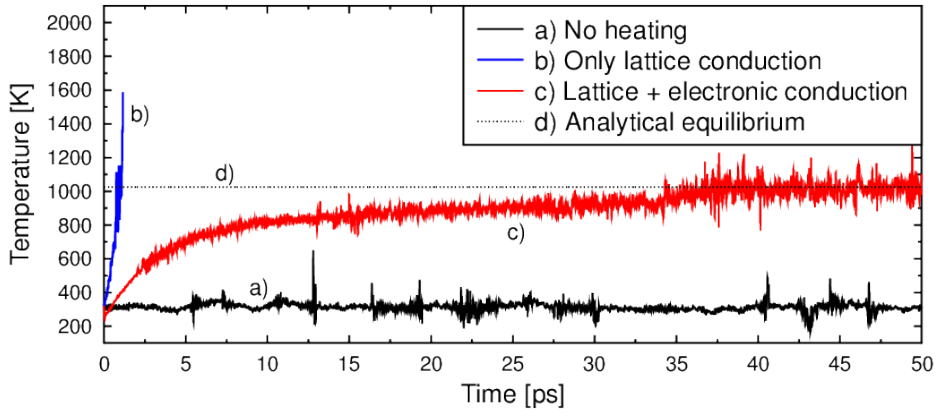

Figure 4.7: Evolution of apex temperature of a tip with final height 13.1 nm and diameter 2 nm when a constant current of density 7.9×10^6 A/nm passes through it. The temperature approaches the analytically predicted value 1033 K only when both lattice and electronic conduction are included.

The KMC step works as follows:

1. Calculate the evaporation probability P_i for each surface atom i based on Eq. (3.11)
2. Calculate the cumulative probability function $F(a) = \sum_{i=1}^{a} P_i$
3. Generate a uniformly random number $r \in (0, 1]$
4. Find atom a to evaporate such that $F(a-1) \leq rF(N) \leq F(a)$, where N is the number of candidate atoms

Because temperature is already explicitly accounted for in Eq. (3.11), the atoms in the system must be in the ground state, *i.e.* relaxed to 0 K in MD, for the above scheme to work correctly; otherwise the effect of temperature would be accounted for twice, since temperature in MD also implicitly affects the binding energy of an atom. Therefore, the system is allowed to relax to this state between evaporations by setting the MD temperature to $T = 0$ K using the MD thermostat. There are, thus, two essentially independent temperatures used in this model: the temperature used in Eq. (3.11), and the MD temperature which should be set to $T = 0$ K.

For Eq. (3.15), the binding energy Λ is given by the MD potential, while the ionisation energy H and work function ϕ are taken as user input. In the model it is always assumed that the atom is evaporated in the same charge state n, taken as the most likely state, also given as user input. Contrary to the case with the direct field evaporation described in Chapter 4.2.4, this scheme will take the charge state of the evaporated atom into consideration.

4.2.7 Calculation of trajectories of evaporated ions

When an atom evaporates as an ion, it is possible to calculate the trajectory of the ion in the electric field. In the current model it is assumed that an ion evaporates at rest (no initial kinetic energy), *i.e.* its velocity is entirely due to the interaction with the electric field. The trajectory is then solved using the velocity-verlet integration scheme [63], calculating the Lorentz force acting on the ion as it moves through the field, and following the motion of the ion until a certain distance above the surface. By recording the time of flight of the ion, as well as its position once it reaches a certain height above the surface, it is possible to simulate hits on a detector screen.

Similarly, it is also possible to calculate the trajectories of ions of an opposite sign heading towards the surface. In this case, it is motivated to give the ions an initial velocity corresponding

to their kinetic energy. The trajectory is calculated until the ion would hit the surface, and the impact position is recorded.

Chapter 5

Application of the model

5.1 Protrusion growth in the presence of a near-surface void

When an electric field is applied to a metal surface, it will introduce a tensile stress due to the interaction between the electric field and the charged surface atomic layer. If impurities are present in the surface they may act as stress concentrators, which enables dislocations to nucleate at these sites. Indeed, the simulations carried out in Publication **V** shows that in the presence of a near-surface void, this results in dislocation-based mass transport towards the surface and the formation of a protrusion on the surface (Fig. 5.1). While this mechanism has not been confirmed by experiments yet, such voids have been observed even in high-purity Cu [86, 87]. It should be noted that in these simulations the strength of the applied electric field has been exaggerated due to the limited time span offered by molecular dynamics. Nevertheless, it validates that the growth mechanism is possible, and that protrusion growth may occur under an applied field, although it remains unclear *e.g.* how fast the process is at realistic field strengths.

Even though the protrusion is free to grow ever taller, limited only by the amount of matter between the surface and the void, its diameter is kept constant as it depends on the diameter of the dislocation nucleation site. This means that the aspect ratio of the protrusion will grow with time. Since the field enhancement at the protrusion apex is proportional to the aspect ratio, it also means that the force acting on the protrusion, and, hence, the protrusion growth rate increases with time (Fig. 5.2). This results in an asymptotic growth, which causes the protrusion to be destroyed catastrophically. The growth and evolution of the protrusion into a potential field emitter is, thus, very fast, and explains why many emitters seem to be unstable

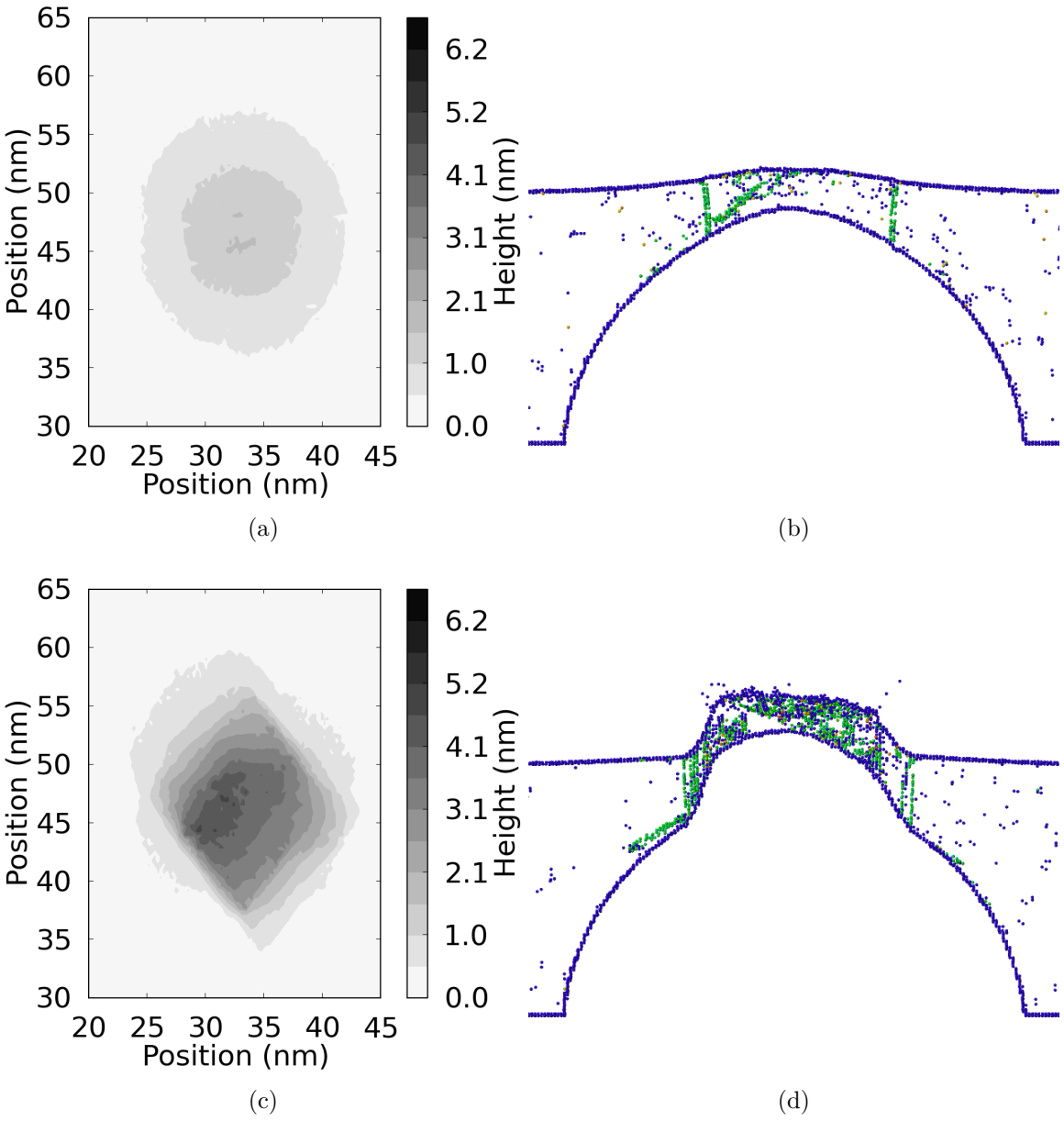

Figure 5.1: Simulation of protrusion growth when a field of 13.4 GV/m is applied on a Cu surface with a void with a radius of 15 nm at depth 6 nm. (a) and (b) show the top view and a slice of the system when stacking faults have formed. (c) and (d) show the same, 14 ps later, when stacking faults are clearly visible. Evaporated atoms are not shown for clarity in a) and c).

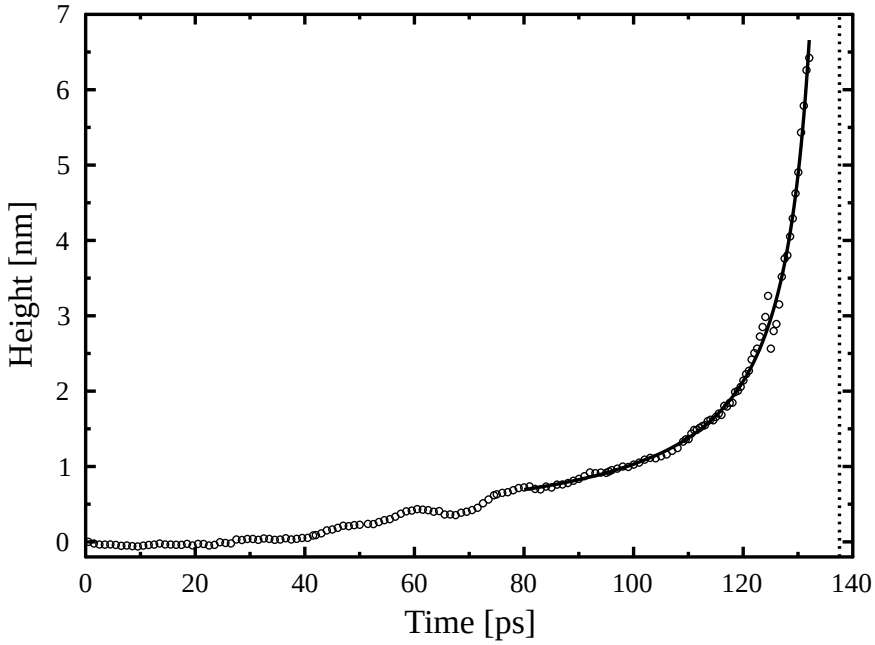

Figure 5.2: Height of a protrusion growing due to the presence of a near-surface void. The growth is asymtotical, with the dashed line indicating the limit.

in experiments (Fig. 5.3). The result is also consistent with results showing that a high electric field is required to activate a field emission site, while a lower field can subsequently be used to trigger emission [16]: a higher field is required to initially break the surface, while emitters can regrow more easily close to sites where this has already occurred. Furthermore, catastrophic growth like this results in a large amount of neutral atoms being released, which contribute to plasma formation as described in Chapter 3.6.

5.2 Effects of resistive heating on a surface protrusion

Due to field enhancement, the field emission current flowing through an emitter will be approximately proportional to its aspect ratio, as per Eq. (3.7). At the same time, the cooling rate is also affected by the aspect ratio, as a tall tip cools less efficiently, while a narrow tip heats more rapidly (due to FSE). Combined, these factors result in the maximum temperature reached in a protrusion only depending on the aspect ratio. Fig. 5.4 shows the temperature reached at the apex of a Cu protrusion at different applied field strengths. Firstly, it is seen that when finite size effects are included, protrusions will reach melting temperature at lower field strengths, due to more efficient heating from the current, and less efficient heat transport away from the protrusion. Secondly, protrusions with the aspect ratio between $30 - 50$ will start to melt at

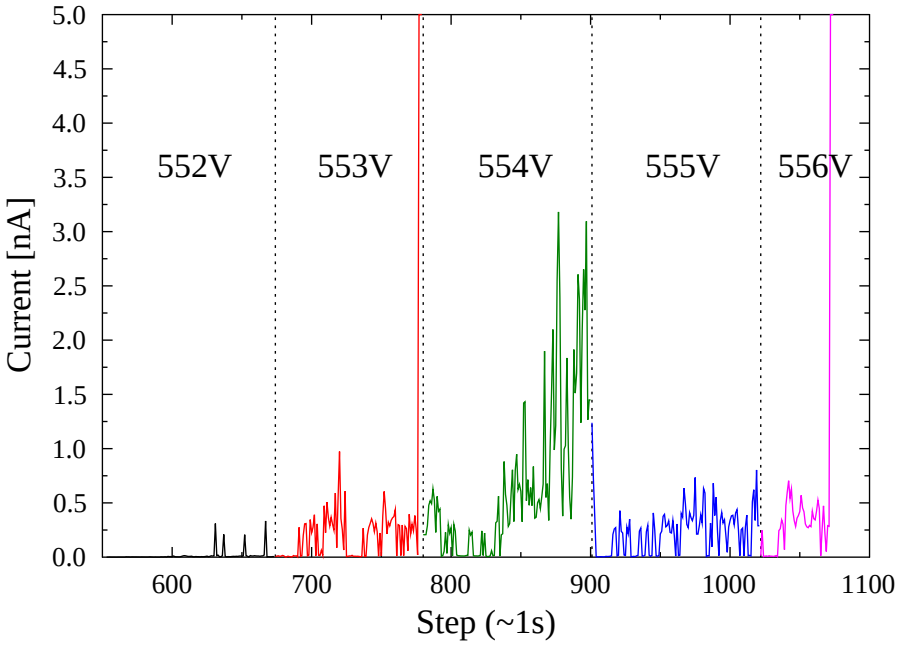

Figure 5.3: Typical measurement of field emission current from a Cu sample at different applied voltages. With the applied voltage 554 V it is seen that the current increases even though the voltage remains unchanged. This indicates that surface modification occurs, which increases the field enhancement, and, thus, the emission current. Data courtesy of Tomoko Muranaka.

relatively modest field strengths, which corresponds well to experimental results where emitters with an aspect ratio in the mentioned range are seen to lead to electric breakdowns [88]. Thus, it seems like the melting of surface protrusions are connected to vacuum breakdowns, possibly by supplying neutral atoms needed to form a plasma [47], as the field evaporation of atoms is greatly enhanced at high temperatures.

In some cases *Rayleigh instability* [89, 90] appeared in simulated protrusions (Fig. 5.5). This can also be another source for neutral atoms to form a plasma, as the resulting necking creates a weak spot, possibly leading to a relatively large chunk of metal to break off. Because of the narrow neck, the field emission current flowing through the protrusion will have a high density there, further weakening the structure at that point. However, Rayleigh instability is a slow process, and, therefore, difficult to simulate using MD, and no simulation of complete breakage of the protrusion was performed.

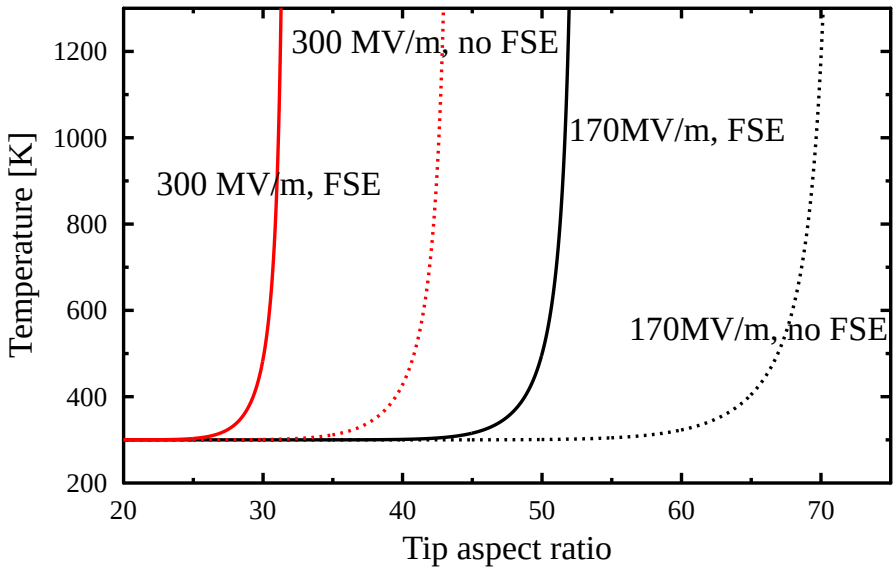

Figure 5.4: Maximum tip temperature as a function of tip aspect ratio when an external electric field is applied. Finite size effects (FSE) are considered for the solid lines, while the effects have been ignored for the dotted lines. The field enhancement factor is assumed to be given by the tip aspect ratio.

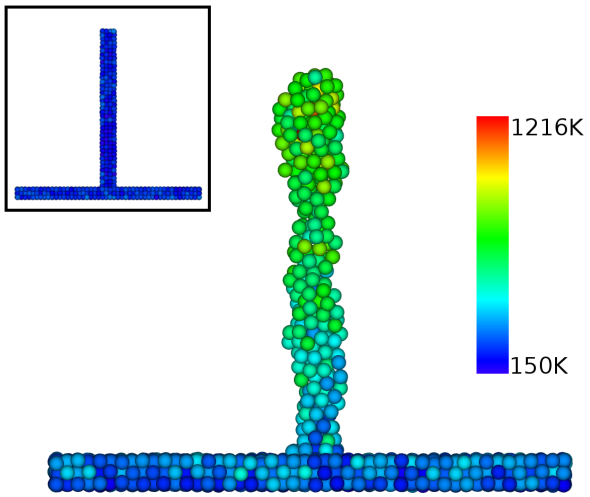

Figure 5.5: Tip shape after resistive heating (inset shows original tip shape after relaxation). The middle part of the tip has become narrower due to Rayleigh instability.

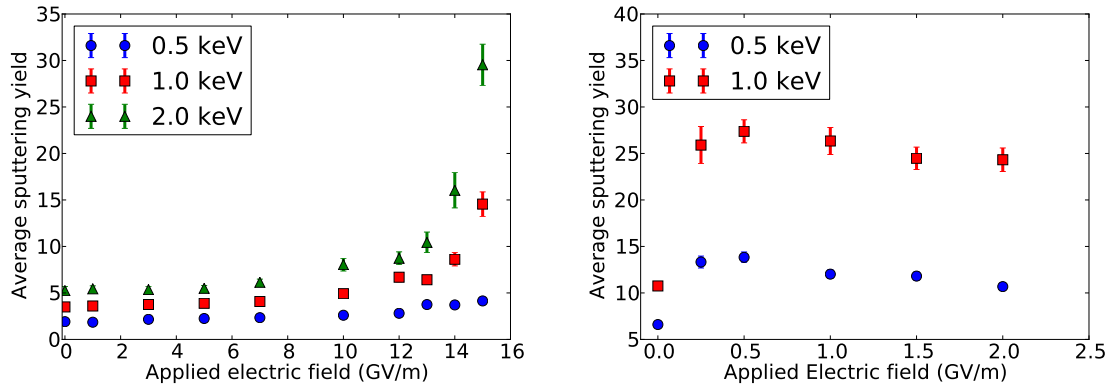

(a) (b)

Figure 5.6: Sputtering yield as a function of electric field for a) a flat Cu surface and b) a nanoprotrusion with a height of 5 nm and a diameter of 2 nm. In case a) it is seen that there is a strong dependence on the electric field, especially as the energy of the incident ion increases. In case b) no such dependence is seen.

5.3 Enhanced sputtering yield under a high electric field

In addition to the mechanical modification of surfaces described above, high electric fields may also play a role in the surface modification mechanisms by ion bombardment. As mentioned in Chapter 3.6, in the presence of a high electric field and a field emission current, evaporated atoms may become ionised and accelerated back towards the surface from where they evaporated. While the energy dependence of the sputtering yield is well known [58], less attention has been paid to the effect of an external electric field even though the sputtering yield under an electric field is of critical importance in *e.g.* simulations of plasma formation [47].

Fig. 5.6a shows the sputtering yield of Cu^+ atom on an atomically flat Cu-surface. The sputtering yield clearly depends on the strength of the electric field, with the effect being more pronounced with incident ions with higher energy, resulting in a sputtering yield several times larger than the non-enhanced yield. The effect is explained by the change in surface morphology after an impact, exposing many loosely bound atoms to the electric field. Additionally, the surface may change in such a way as to cause field enhancement and the enhanced local field will then cause evaporation of atoms from the surface. Thus, the sputtering yield is higher in the presence of an electric field compared with no field.

It is known from previous studies that the sputtering yield can be greatly enhanced by finite size effects, such as when an ion hits a nanosized feature on the surface [91]. The same effect can be observed also in the case of nanoprotrusions under an electric field. To measure the

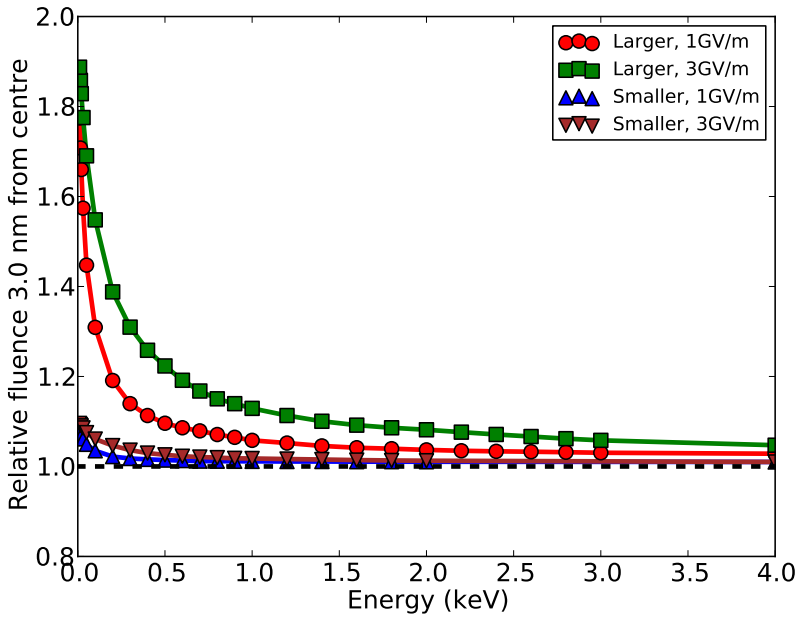

Figure 5.7: The size of a protrusion has a marked effect on how effectively ions are focused towards it. The graph shows the relative fluence within 3 nm from the centre of a protrusion. Two different sizes were investigated: the smaller protrusion was of height 5 nm and diameter 1 nm and the larger one of height 10 nm and diameter 4 nm.

sputtering yield the field is kept low enough not to cause spontaneous field evaporation from the protrusion apex, where the field can be enhanced significantly. Thus, only relatively modest values can be used for the applied field. Fig. 5.6b shows the sputtering yield of a Cu^+ ion on a Cu nanoprotrusion with a height of 5 nm and diameter 2 nm. It is seen that the sputtering yield remains fairly constant with increasing field. The lack of field dependence is explained by the fact that only the very apex, and, thus, a limited number of atoms, is affected by the strong field, while atoms elsewhere remain unaffected. Since the apex atoms have a high sputtering probability even without the applied field, increasing the field does not make sputtering more probable.

In addition to increasing the sputtering yield, nanoprotrusions may also serve to increase the local ion fluence around them, by distorting the electric field, and, thus, the trajectories of the incoming ions. Fig. 5.7 shows the relative local fluence around a protrusion with a given size, compared with the unmodified applied fluence. Highly energetic ions are affected less by the presence of the protrusions, since they have a high initial velocity, and the distortion in the electric field is not strong enough to significantly alter their trajectory. Low energy ions, on the other hand, are easily deflected towards the protrusion.

5.4 Distortions in ion trajectories due to changes in surface morphology

As shown in Fig. 5.7 the presence of geometric features on a surface can alter the trajectories of ions, due to the change in the shape of the local electric field. If the kinetic energy of the ions is small enough, even small scale modification of the surface is enough to alter trajectories of ions [53]. Thus, the previously mentioned protrusion growth and surface modification due to ion irradiation, may have a large effect on the trajectories of evaporating ions, as these typically have a low initial kinetic energy near the surface where the local field is distorted the most.

The aberration in the trajectory can have a significant effect in some applications, such as atom probe tomography (APT), where the trajectory must be known with high accuracy to obtain a good reconstruction [21, 92–94]. Additionally, the order in which ions evaporate from a sample is of critical importance in reconstructions, since depth information is deduced from this [92]. It is often assumed that evaporation occurs one atomic layer at a time. However, when a sample consists of elements with vastly different evaporation fields, this assumption may not hold [53]. Even state-of-the-art APT reconstruction algorithms are unable to accurately compensate for this effect. However, with an increased understanding of how changes on the atomic level affects trajectories, it may be possible to develop more advanced reconstruction protocols, and, thus, vastly improve the resolution of APT.

Trajectory aberrations are clearly visible in simulated detector data Fig. 5.8. In comparison with a completely flat Cu surface (Fig. 5.8a) trajectory aberrations result in severe artifacts in the presence of a pit (Fig. 5.8b) or an Fe inclusion (Fig. 5.8c) on the surface. In fact, both pits and inclusions may result in similar looking detector patterns, with a lower number of ions hitting the middle of the detector. For a pit, this is simply explained by a lack of atoms at that point on the sample. For the inclusion, the situation is more complex.

Fig. 5.9a illustrates how trajectories of evaporated ions from a Cu surface with a small Fe inclusion are bent due to the marks left on a surface by previously evaporated atoms. In the initial state the surface is very smooth, leading to just a small deviation in trajectories. However, as the surface becomes more rough there is an increase in trajectory aberrations. Additionally, since Fe has a higher evaporation field than Cu, the Fe atoms start forming a protrusion on the surface as the surrounding Cu matrix is evaporated before the Fe (Fig. 5.10). The inclusion distorts the local electric field in such a way that evaporating ions are accelerated outwards from it. Once a full layer has been removed, little surface roughness remains, and the aberration in trajectories decreases.

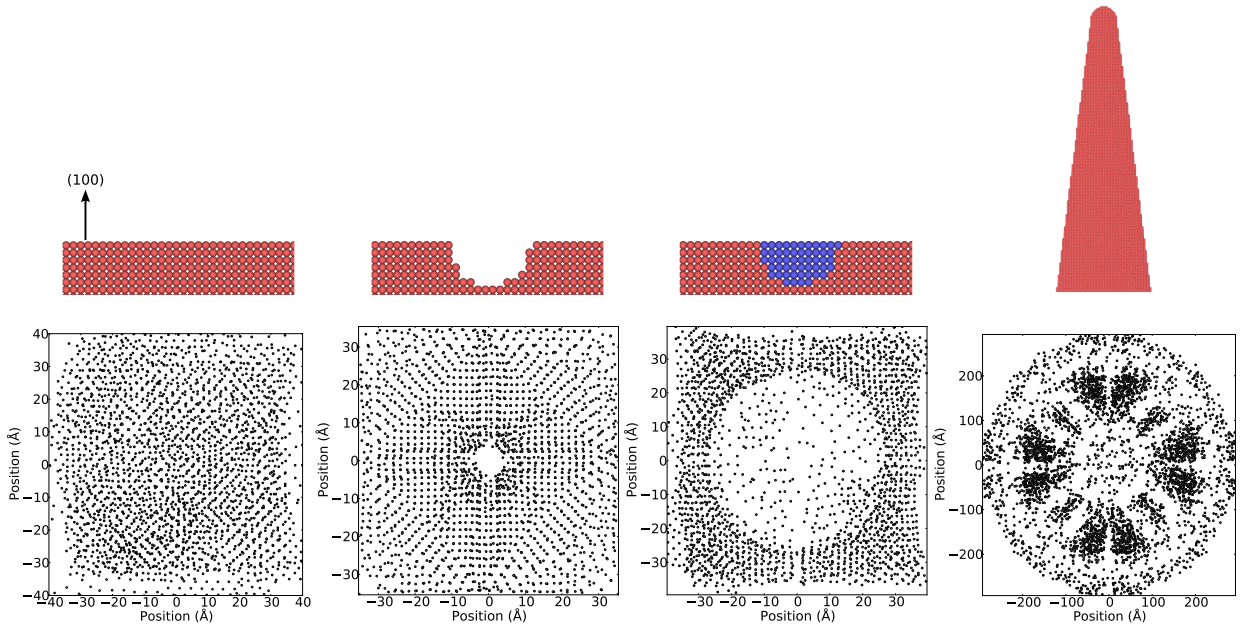

(a) (b) (c) (d)

Figure 5.8: Simulated detector hits in the case of a) flat Cu surface b) flat Cu surface with a pit and c) flat Cu surface with an Fe inclusion. Case d) shows detector hits for a sample of the form "hemisphere-on-a-post" as used in APT experiments. The clustered hits in d) correspond to crystallographic poles. The total number of evaporation events in cases a)-c) is 2400, corresponding to 3 atomic monolayers. For case d) 3680 evaporation events were simulated.

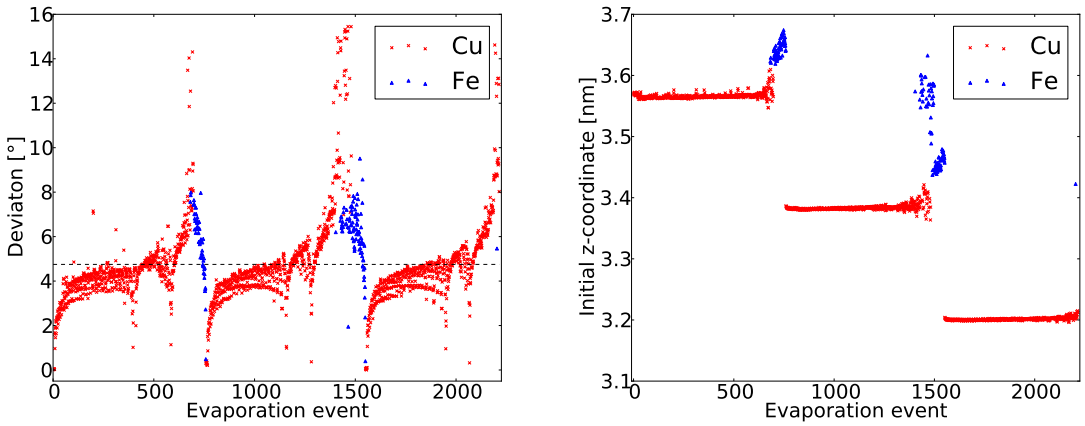

(a) (b)

Figure 5.9: a) Deviation from a straight path of evaporated ions in the case of a Fe inclusion in a Cu matrix. b) The initial height-position of evaporated atoms in the same case.

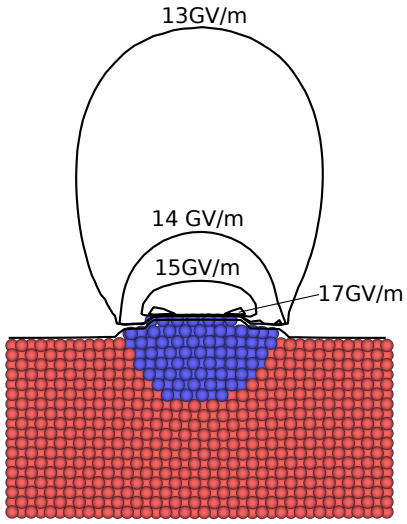

Figure 5.10: An Fe protrusion is formed when the Cu surrounding an Fe inclusion is evaporated before the Fe. The electric field is then distorted and enhanced around the protrusion.

APT samples are usually prepared in the shape of a hemisphere on a cone to obtain sufficient field enhancement to facilitate field evaporation of ions from the specimen [95]. Using our model, it is possible to simulate such a sample under conditions similar to actual APT experiments, and apply the same reconstruction algorithm [92] to the simulated data as is applied in actual APT experiments. The reconstructed shape can then be compared with the actual initial shape of the sample, which is known exactly in simulations (Fig. 5.11). The simulations shows that while the reconstructed sample is of similar size and shape of the original one, reconstruction artifacts are also visible. Notably the reconstruction algorithm fails to reproduce the step edges on the sample. However, as APT normally has a detector efficiency [96, 97] of $\approx 60\% - 85\%$ such precision may not be reachable in actual experiments in any case.

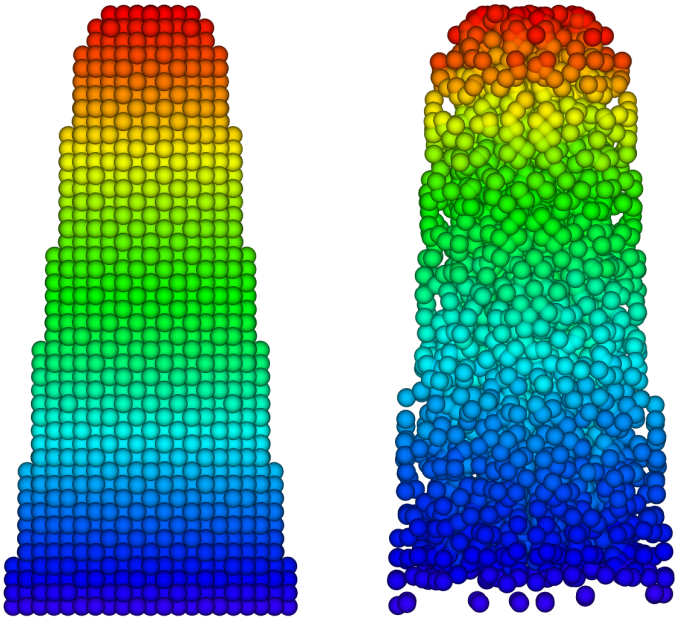

(a) (b)

Figure 5.11: Part of the original tip and the reconstructed model based on 3860 evaporation events. The colour indicates the original position of an atom along the z-axis. The reconstructed model is similar in shape and size to the original.

Chapter 6

Conclusions and outlook

The main result of this thesis is the study of several electronic effects by extending classical molecular dynamics, as presented in Chapter 4. This hybrid electrodynamics-molecular dynamics-Monte Carlo model enables the simulation of a wide variety of processes involving high electric fields and metal surfaces, which has not been possible using previous methods. The model is fully dynamic, meaning that the system is allowed to evolve freely. Although most of the result presented in this thesis is related to Cu or Fe in Cu, the method can be used for any conducting material for which there exists an interatomic potential for MD simulations.

The implementation includes an electric field solver based on the multigrid method, which gives good results while simultaneously being efficient. Performance is also improved by only solving the electric field around an area of interest if it can be assumed that the effect of the field is small elsewhere. Using the calculated field, each atom facing the electric field is given an induced charge based on Gauss' law. While the current solver works under the assumption that there is a negligible amount of free charge in the electric field, this can be extended in the future.

The effect of field emission when a negative field is applied to a metal surface is implemented via the Fowler-Nordheim equation, including a temperature correction factor. The temperature of the system is then adjusted to account for resistive heating by solving the heat equation. Electronic thermal conductivity is also included in the solution, providing for a more realistic cooling rate than provided by pure MD where only thermal conductivity is accounted for. A more advanced general thermal field emission model, including the Nottingham effect, could be employed to further increase the accuracy of the model over a larger range of temperatures and field strengths.

Field evaporation is included in the model either directly, by a sufficiently high force pulling an atom away from the surface, or via a Monte Carlo step where an atom is picked at random, based on its evaporation probability, and then removed from the system. Currently in the MC step it is assumed that an atom always evaporates into its most likely charge state. Future work could improve this relatively easily by considering the ionisation potential of different charge states.

Using the method it was observed in simulations how a void beneath a Cu surface can lead to the growth of a surface protrusion when a high electric field is applied. The stress induced by the electric field triggers dislocation nucleation and motion causing mass transport towards the surface. Because of a positive feedback loop the growth is very rapid and results in catastrophic breakage of the protrusion, which may explain the instability observed in field emission measurement experiments.

The performed simulations also show that changes in surface morphology on the atomic level affects the trajectories of subsequently evaporated ions, resulting in visible aberrations in simulated APT experiments. The simulation code developed for this thesis can be used to study this effect more closely to develop more accurate reconstruction protocols, where these kind of effects are taken into consideration. This is of high importance, since the lack of knowledge about the trajectories is currently limiting the resolution of APT.

The work presented in this study is mostly theoretical in nature. It is therefore, the hope of the author, that the simulation methods presented here will in future be applied to cases which can easily be compared with experiments, to investigate how good our current understanding of the processes presented here is.

Acknowledgements

I wish to thank the former head of the Department of Physics at the University of Helsinki, Prof. Juhani Keinonen, the current head Prof. Hannu Koskinen, as well as the head of the Accelerator Laboratory, Prof. Jyrki Räisänen, for providing the facilities for the research presented in this thesis. Financial support from Waldemar von Frenckells stiftelse and the Chancellor's Travel Grant are gratefully acknowledged.

I am forever grateful for the advice and encouragement given to me by my supervisor, Doc. Flyura Djurabekova, during this PhD project. Thanks to her guidance I was able to pursue research topics that personally interested me, while at the same time making sure I did not get lost on the way. I could not have wished for anything better now at the start of my scientific career. Thank you.

I would also like to thank Prof. Kai Nordlund, whose optimistic outlook on both science and life in general has served as great inspiration during these years.

This work has partly been the result of fruitful collaboration with CERN. I would especially like to thank Dr Walter Wuench and Sergio Calatroni for the many fruitful discussions, and for allowing me to stay at CERN to get acquainted with the experimental wquipment there. For the work related to APT, I wish to thank Claudia Müller and Stephan Gerstl.

During my work on this thesis my office mates have always been of great support, from trivial tips on software usage, to more fundamental discussions about science. Thank you Aarne, Avaz, Ville and Vahur for providing such a pleasant and interesting work environment. I also wish to extend my thanks to all my other friends at the accelerator lab, both current co-workers and those who have already moved elsewhere, for creating a welcoming atmosphere where I've always felt at home. The topics of our coffee break discussions will never be forgotten.

Finally, I wish to thank my family for always believing in me and making all this possible.

Helsinki, February 28th, 2014
Stefan Parviainen

Bibliography

1. M. Aicheler, P. Burrows, M. Draper, T. Garvey, P. Lebrun, K. Peach, N. Phinney, H. Schmickler, D. Schulte, and N. Tog, eds., *A Multi-TeV linear collider based on CLIC technology: CLIC Conceptual Design Report*. CERN, 2012.

2. A. Grudiev, S. Calatroni, and W. Wuensch, "New local field quantity describing the high gradient limit of accelerating structures," *Physical Review Special Topics - Accelerators and Beams*, vol. 12, pp. 102001+, Oct. 2009.

3. A. T. Hubbard, *The Handbook of Surface Imaging and Visualization*. Taylor & Francis, 1995.

4. E. W. Müller and K. Bahadur, "Field Ionization of Gases at a Metal Surface and the Resolution of the Field Ion Microscope," *Physical Review*, vol. 102, pp. 624–631, 1956.

5. E. W. Müller, "Field Ion Microscopy," *The Physics Teacher*, vol. 4, pp. 53–56, Sept. 2006.

6. T. F. Kelly, D. J. Larson, K. Thompson, R. L. Alvis, J. H. Bunton, J. D. Olson, and B. P. Gorman, "Atom Probe Tomography of Electronic Materials," *Annual Review of Materials Research*, vol. 37, no. 1, pp. 681–727, 2007.

7. D. N. Seidman, "Three-Dimensional Atom-Probe Tomography: Advances and Applications," *Annual Review of Materials Research*, vol. 37, no. 1, pp. 127–158, 2007.

8. T. F. Kelly and D. J. Larson, "Atom Probe Tomography 2012," *Annual Review of Materials Research*, vol. 42, no. 1, pp. 1–31, 2012.

9. T. J. Wilkes, J. M. Titchmarsh, G. D. W. Smith, D. A. Smith, R. F. Morris, S. Johnston, T. J. Godfrey, and P. Birdseye, "The fracture of field-ion microscope specimens," *Journal of Physics D: Applied Physics*, vol. 5, pp. 2226+, Dec. 1972.

10. K. F. Russell, M. K. Miller, R. M. Ulfig, and T. Gribb, "Performance of local electrodes in the local electrode atom probe," *Ultramicroscopy*, vol. 107, pp. 750–755, Sept. 2007.

11. F. Liu and H.-O. Andrén, "Effects of laser pulsing on analysis of steels by atom probe tomography," *Ultramicroscopy*, vol. 111, pp. 633–641, May 2011.

12. K. L. Jensen, Y. Y. Lau, D. W. Feldman, and P. G. O'Shea, "Electron emission contributions to dark current and its relation to microscopic field enhancement and heating in accelerator

structures," *Physical Review Special Topics - Accelerators and Beams*, vol. 11, pp. 081001+, Aug. 2008.

13. S. T. Purcell, P. Vincent, C. Journet, and V. T. Binh, "Hot Nanotubes: Stable Heating of Individual Multiwall Carbon Nanotubes to 2000 K Induced by the Field-Emission Current," *Physical Review Letters*, vol. 88, pp. 105502+, Feb. 2002.

14. R. Behrisch, "Surface Erosion by Electrical Arcs," in *Physics of Plasma-Wall Interactions in Controlled Fusion* (D. E. Post and R. Behrisch, eds.), pp. 495–513, New York: Plenum Press, 1986.

15. D. W. Williams and W. T. Williams, "Field-emitted current necessary for cathode-initiated vacuum breakdown," *Journal of Physics D: Applied Physics*, vol. 5, pp. 280+, Feb. 1972.

16. A. Navitski, S. Lagotzky, D. Reschke, X. Singer, and G. Müller, "Field emitter activation on cleaned crystalline niobium surfaces relevant for superconducting rf technology," *Phys. Rev. ST Accel. Beams*, vol. 16, p. 112001, 2013.

17. T. Muranaka, T. Blom, K. Leifer, V. Ziemann, A. Navitski, and G. Müller, "Analysis of a copper sample for the CLIC ACS study in a field emission scanning microscope," Tech. Rep. CERN-OPEN-2012-009. CLIC-Note-935, Uppsala U., Uppsala, Dec. 2011.

18. A. Descoeudres, Y. Levinsen, S. Calatroni, M. Taborelli, and W. Wuensch, "Investigation of the dc vacuum breakdown mechanism," *Physical Review Special Topics - Accelerators and Beams*, vol. 12, pp. 092001+, Sept. 2009.

19. O. L. Golubev and V. N. Shrednik, "Preequilibrium thermofield microprotrusions as effective field point sources of electrons and ions," *Technical Physics*, vol. 50, no. 9, pp. 1217–1222, 2005.

20. M. P. Allen and D. J. Tildesley, *Computer Simulation of Liquids*. Oxford science publications, Oxford University Press, USA, June 1989.

21. I. Arslan, E. A. Marquis, M. Homer, M. A. Hekmaty, and N. C. Bartelt, "Towards better 3-D reconstructions by combining electron tomography and atom-probe tomography," *Ultramicroscopy*, vol. 108, pp. 1579–1585, Nov. 2008.

22. M. K. Miller, T. Kelly, K. Rajan, and S. P. Ringer, "The future of atom probe tomography," *Materials Today*, vol. 15, pp. 158–165, Apr. 2012.

23. K. Nordlund, M. Ghaly, R. S. Averback, M. Caturla, T. Diaz de la Rubia, and J. Tarus, "Defect production in collision cascades in elemental semiconductors and fcc metals," *Phys. Rev. B*, vol. 57, no. 13, pp. 7556–7570, 1998.

24. M. Ghaly, K. Nordlund, and R. S. Averback, "Molecular dynamics investigations of surface damage produced by kev self-bombardment of solids," *Phil. Mag. A*, vol. 79, no. 4, p. 795, 1999.

25. J. Shipman, J. Wilson, and C. Higgins, *An Introduction to Physical Science*. Textbooks Available with Cengage Youbook, Cengage Learning, 2012.

26. N. W. Ashcroft and N. D. Mermin, *Solid State Physics*. Cengage Learning India Private Limited, 2011.

27. M. Clugston and R. Flemming, *Advanced Chemistry*. A new mainstream text for the new specifications, OUP Oxford, 2000.

28. B. S. Mitchell, *An Introduction to Materials Engineering and Science for Chemical and Materials Engineers*. Wiley, 2004.

29. J. S. Blakemore, *Solid State Physics*. Cambridge University Press, 1985.

30. J. D. Jackson, *Classical Electrodynamics*. John Wiley & Sons, second edition ed., 1975.

31. T. Ono, T. Sasaki, J. Otsuka, and K. Hirose, "First-principles study on field evaporation of surface atoms from W(011) and Mo(011) surfaces," *Surface Science*, vol. 577, pp. 42–46, Feb. 2005.

32. R. G. Forbes, C. J. Edgcombe, and U. Valdrè, "Some comments on models for field enhancement," *Ultramicroscopy*, vol. 95, pp. 57–65, May 2003.

33. R. G. Forbes, "Screened field enhancement factor for a tall closely spaced array of identical conducting posts and implications for Fowler-Nordheim-type equations," *Journal of Applied Physics*, vol. 111, no. 9, 2012.

34. R. Miller, Y. Y. Lau, and J. H. Booske, "Schottky's conjecture on multiplication of field enhancement factors," *Journal of Applied Physics*, vol. 106, no. 10, 2009.

35. C. J. Edgcombe and U. Valdrè, "Microscopy and computational modelling to elucidate the enhancement factor for field electron emitters," *Journal of Microscopy*, vol. 203, pp. 188–194, Aug. 2001.

36. P. Lazić and B. N. J. Persson, "Surface-roughness–induced electric-field enhancement and triboluminescence," *EPL (Europhysics Letters)*, pp. 46003+, Aug. 2010.

37. O. W. Richardson, *On the Negative Radiation from Hot Platinum*. University Press, 1901.

38. A. Einstein, "Über einen die Erzeugung und Verwandlung des Lichtes betreffenden heuristischen Gesichtspunkt," *Annalen der Physik*, vol. 322, no. 6, pp. 132–148, 1905.

39. R. H. Fowler and L. Nordheim, "Electron Emission in Intense Electric Fields," *Royal Society of London Proceedings Series A*, vol. 119, pp. 173–181, May 1928.

40. R. G. Forbes and J. H. B. Deane, "Reformulation of the standard theory of Fowler–Nordheim tunnelling and cold field electron emission," *Proceedings of the Royal Society A: Mathematical, Physical and Engineering Science*, vol. 463, pp. 2907–2927, Nov. 2007.

41. R. G. Forbes, "Use of energy-space diagrams in free-electron models of field electron emission," *Surface and Interface Analysis*, vol. 36, no. 5-6, pp. 395–401, 2004.

42. E. L. Murphy and R. H. Good, "Thermionic Emission, Field Emission, and the Transition Region," *Physical Review Online Archive (Prola)*, vol. 102, pp. 1464–1473, June 1956.

43. J. W. Gadzuk and E. W. Plummer, "Field Emission Energy Distribution (FEED)," *Reviews of Modern Physics*, vol. 45, pp. 487–548, July 1973.

44. K. L. Jensen, "General formulation of thermal, field, and photoinduced electron emission," *Journal of Applied Physics*, vol. 102, no. 2, 2007.

45. J. P. Barbour, W. W. Dolan, J. K. Trolan, E. E. Martin, and W. P. Dyke, "Space-Charge Effects in Field Emission," *Physical Review Online Archive (Prola)*, vol. 92, pp. 45–51, Oct. 1953.

46. A. Rokhlenko, K. L. Jensen, and J. L. Lebowitz, "Space charge effects in field emission: One dimensional theory," *Journal of Applied Physics*, vol. 107, no. 1, pp. 014904+, 2010.

47. H. Timko, K. Matyash, R. Schneider, F. Djurabekova, K. Nordlund, A. Hansen, A. Descoeudres, J. Kovermann, A. Grudiev, W. Wuensch, S. Calatroni, and M. Taborelli, "A One-Dimensional Particle-in-Cell Model of Plasma Build-Up in Vacuum Arcs," *Contributions to Plasma Physics*, vol. 51, no. 1, pp. 5–21, 2011.

48. Z. M. Zhang, *Nano/Microscale Heat Transfer*. McGraw Hill professional, McGraw-Hill, 2007.

49. W. Liu, Y. Yang, and M. Asheghi, "Thermal and electrical characterization and modeling of thin copper layers," in *Thermal and Thermomechanical Phenomena in Electronics Systems, 2006. ITHERM '06. The Tenth Intersociety Conference on*, pp. 1171–1176, IEEE, May 2006.

50. A. E. Yarimbiyik, H. A. Schafft, R. A. Allen, M. E. Zaghloul, and D. L. Blackburn, "Modeling and simulation of resistivity of nanometer scale copper," *Microelectronics Reliability*, vol. 46, no. 7, 2006.

51. F. M. Charbonnier, R. W. Strayer, L. W. Swanson, and E. E. Martin, "Nottingham Effect in Field and T-F Emission: Heating and Cooling Domains, and Inversion Temperature," *Physical Review Letters*, vol. 13, pp. 397–401, Sept. 1964.

52. J. Paulini, T. Klein, and G. Simon, "Thermo-field emission and the Nottingham effect," *Journal of Physics D: Applied Physics*, vol. 26, pp. 1310+, Aug. 1993.

53. B. Gault, M. P. Moody, J. M. Cairney, and S. P. Ringer, *Atom Probe Microscopy*. Springer Series in Materials Science, Springer, 2012.

54. T. T. Tsong, *Atom-Probe Field Ion Microscopy: Field Ion Emission, and Surfaces and Interfaces at Atomic Resolution*. Cambridge University Press, 2005.

55. H. Timko, F. Djurabekova, K. Nordlund, L. Costelle, K. Matyash, R. Schneider, A. Toerklep, G. A. Izquierdo, A. Descoeudres, S. Calatroni, M. Taborelli, and W. Wuensch, "Mechanism of surface modification in the plasma-surface interaction in electrical arcs," *Physical Review B*, vol. 81, pp. 184109+, May 2010.

56. P. Sigmund, "Theory of Sputtering. I. Sputtering Yield of Amorphous and Polycrystalline Targets," *Physical Review Online Archive (Prola)*, vol. 184, pp. 383–416, Aug. 1969.

57. N. Matsunami, Y. Yamamura, Y. Itikawa, N. Itoh, Y. Kazumata, S. Miyagawa, K. Morita, R. Shimizu, and H. Tawara, "Energy dependence of the ion-induced sputtering yields of monatomic solids," *Atomic Data and Nuclear Data Tables*, vol. 31, pp. 1–80, July 1984.

58. K. Grais, A. A. Shaltout, S. S. Ali, R. M. Boutros, K. M. El-behery, and Z. A. El-Sayed, "A new formula for sputtering yield as function of ion energies at normal incidence," *Physica B: Condensed Matter*, vol. 405, pp. 1775–1781, Apr. 2010.

59. R. G. Forbes, "Field evaporation theory: a review of basic ideas," *Applied Surface Science*, vol. 87-88, pp. 1–11, Mar. 1995.

60. E. W. Müller, "Field Desorption," *Physical Review Online Archive (Prola)*, vol. 102, pp. 618–624, May 1956.

61. R. Gomer, "Field Desorption," *The Journal of Chemical Physics*, vol. 31, no. 2, pp. 341–345, 1959.

62. B. J. Alder and T. E. Wainwright, "Phase Transition for a Hard Sphere System," *The Journal of Chemical Physics*, vol. 27, pp. 1208–1209, Aug. 1957.

63. W. C. Swope, H. C. Andersen, P. H. Berens, and K. R. Wilson, "A computer simulation method for the calculation of equilibrium constants for the formation of physical clusters of molecules: Application to small water clusters," *The Journal of Chemical Physics*, vol. 76, no. 1, 1982.

64. C. W. Gear, *Numerical Initial Value Problems in Ordinary Differential Equations*. Prentice-Hall series in automatic computation, Prentice-Hall, 1971.

65. M. Born and R. Oppenheimer, "Zur Quantentheorie der Molekeln," *Annalen der Physik*, vol. 389, no. 20, 1927.

66. K. Nordlund, "Molecular dynamics simulation of ion ranges in the 1–100 keV energy range," *Computational Materials Science*, vol. 3, pp. 448–456, Mar. 1995.

67. H. J. C. Berendsen, J. P. M. Postma, W. F. van Gunsteren, A. DiNola, and J. R. Haak, "Molecular dynamics with coupling to an external bath," *The Journal of Chemical Physics*, vol. 81, pp. 3684–3690, Oct. 1984.

68. S. Nosé, "A unified formulation of the constant temperature molecular dynamics methods," *The Journal of Chemical Physics*, vol. 81, no. 1, pp. 511–519, 1984.

69. W. G. Hoover, "Canonical dynamics: Equilibrium phase-space distributions," *Physical Review A*, vol. 31, pp. 1695–1697, Mar. 1985.

70. H. C. Andersen, "Molecular dynamics simulations at constant pressure and/or temperature," *The Journal of Chemical Physics*, vol. 72, pp. 2384–2393, July 2008.

71. M. S. Daw, S. M. Foiles, and M. I. Baskes, "The embedded-atom method: a review of theory and applications," *Mat. Sci. Rep.*, vol. 9, p. 251, 1993.

72. M. J. Sabochick and N. Q. Lam, "Radiation-induced amorphization of ordered intermetallic compounds cuti, $cuti_2$, and $cu_4$$ti_3$: A molecular-dynamics study," *Physical Review B*, vol. 43, pp. 5243–5252, Mar. 1991.

73. Y. Mishin, M. J. Mehl, D. A. Papaconstantopoulos, A. F. Voter, and J. D. Kress, "Structural stability and lattice defects in copper: Ab initio, tight-binding, and embedded-atom calculations," *Physical Review B*, vol. 63, p. 224106, May 2001.

74. R. C. Pasianot and L. Malerba, "Interatomic potentials consistent with thermodynamics: The Fe–Cu system," *Journal of Nuclear Materials*, vol. 360, pp. 118–127, Feb. 2007.

75. M. I. Mendelev, S. Han, D. J. Srolovitz, G. J. Ackland, D. Y. Sun, and M. Asta, "Development of new interatomic potentials appropriate for crystalline and liquid iron," *Philosophical Magazine*, vol. 83, pp. 3977–3994, Dec. 2003.

76. S. Pronk, S. Páll, R. Schulz, P. Larsson, P. Bjelkmar, R. Apostolov, M. R. Shirts, J. C. Smith, P. M. Kasson, D. van der Spoel, B. Hess, and E. Lindahl, "GROMACS 4.5: a high-throughput and highly parallel open source molecular simulation toolkit," *Bioinformatics*, vol. 29, pp. 845–854, Apr. 2013.

77. S. Plimpton, "Fast Parallel Algorithms for Short-Range Molecular Dynamics," *Journal of Computational Physics*, vol. 117, pp. 1–19, Mar. 1995.

78. J. Ziegler and J. Biersack, "The Stopping and Range of Ions in Matter," in *Treatise on Heavy-Ion Science* (Bromley, ed.), pp. 93–129, Springer US, 1985.

79. C. P. Flynn and R. S. Averback, "Electron-phonon interactions in energetic displacement cascades," *Physical Review B*, vol. 38, pp. 7118–7120, Oct. 1988.

80. W. H. Press, S. A. Teukolsky, W. T. Vetterling, and B. P. Flannery, *Numerical Recipes 3rd Edition*. Cambridge University Press, 3 ed., 2007.

81. S. Nakamura, *Applied Numerical Methods in C*. Prentice Hall, 1993.

82. W. Briggs and S. McCormick, *Multigrid Methods*. Frontiers in Applied Mathematics, Society for Industrial and Applied Mathematics, 1987.

83. T. T. Tsong, "Effects of an electric field in atomic manipulations," *Physical Review B*, vol. 44, pp. 13703–13710, Dec. 1991.

84. C. E. Schuster, M. G. Vangel, and H. A. Schafft, "Improved estimation of the resistivity of pure copper and electrical determination of thin copper film dimensions," *Microelectronics Reliability*, vol. 41, pp. 239–252, Feb. 2001.

85. K. A. Fichthorn and W. H. Weinberg, "Theoretical foundations of dynamical Monte Carlo simulations," *J. Chem. Phys.*, vol. 95, pp. 1090–1096, July 1991.

86. M. Kato, "The production of ultrahigh-purity copper for advanced applications," *JOM*, vol. 47, no. 12, pp. 44–46, 1995.

87. T. Muranaka, T. Blom, K. Leifer, and V. Ziemann, "In-situ experiments of vacuum discharge using scanning electron microscopes," Tech. Rep. EuCARD-CON-2011-022, Uppsala U., 2011.

88. A. Descoeudres, T. Ramsvik, S. Calatroni, M. Taborelli, and W. Wuensch, "dc breakdown conditioning and breakdown rate of metals and metallic alloys under ultrahigh vacuum," *Physical Review Special Topics - Accelerators and Beams*, vol. 12, pp. 032001+, Mar. 2009.

89. L. Rayleigh, "On the capillary phenomena of jets," *Proc. Roy. Soc. London*, vol. 29, pp. 71–89, 1879.

90. M. E. T. Molares, A. G. Balogh, T. W. Cornelius, R. Neumann, and C. Trautmann, "Fragmentation of nanowires driven by Rayleigh instability," *Applied Physics Letters*, vol. 85, no. 22, pp. 5337–5339, 2004.

91. Z. Xue-Qing, X. Jian-Ming, and W. Yu-Gang, "Damage of low-energy ion irradiation on copper nanowire: molecular dynamics simulation," *Chinese Physics B*, vol. 19, pp. 036102+, Mar. 2010.

92. P. Bas, A. Bostel, B. Deconihout, and D. Blavette, "A general protocol for the reconstruction of 3D atom probe data," *Applied Surface Science*, vol. 87-88, pp. 298–304, Mar. 1995.

93. B. P. Geiser, D. J. Larson, E. Oltman, S. Gerstl, D. Reinhard, T. F. Kelly, and T. J. Prosa, "Wide-Field-of-View Atom Probe Reconstruction," *Microscopy and Microanalysis*, vol. 15, no. Supplement S2, pp. 292–293, 2009.

94. B. Gault, D. Haley, F. de Geuser, M. P. Moody, E. A. Marquis, D. J. Larson, and B. P. Geiser, "Advances in the reconstruction of atom probe tomography data," *Ultramicroscopy*, vol. 111, pp. 448–457, May 2011.

95. D. J. Larson, K. Thompson, D. Lawrence, S. L. P. Kostrna, T. J. Prosa, R. M. Ulfig, and T. F. Kelly, "Advances in Specimen Preparation for Atom Probe Tomography," in *Vacuum Nanoelectronics Conference, 2006 and the 2006 50th International Field Emission Symposium., IVNC/IFES 2006. Technical Digest. 19th International*, pp. 537–538, IEEE, July 2006.

96. M. Hellsing and L. Karlsson, "Detection efficiency in atom-probe time-of-flight mass spectrometry," *Journal of Physics E: Scientific Instruments*, vol. 19, pp. 276+, Apr. 1986.

97. B. Deconihout, P. Gerard, M. Bouet, and A. Bostel, "Improvement of the detection efficiency of channel plate electron multiplier for atom probe application," *Applied Surface Science*, vol. 94-95, pp. 422–427, Mar. 1996.